Chirogenesis in solid state and spontaneous resolution

Reiko Oda, Peizhao Liu, Elizabeth Hillard, Patrick Rosa, Sylvain Nlate, Yutaka Okazaki, Emilie Pouget, Yann Battie, Thierry Buffeteau

6 Chirogenesis in Solid State and Spontaneous Resolution

Reiko Oda,* Peizhao Liu, Elizabeth Hillard,† Patrick Rosa,† Sylvain Nlate,* Yutaka Okazaki,‡ Emilie Pouget,* Yann Battie§ and Thierry Buffeteau¶

*Institute of Chemistry and Biology of Membranes and Nanoobjects, UMR 5248 CNRS, Université de Bordeaux, INP, IECB, Pessac, France
†CNRS, Univ. Bordeaux, Bordeaux INP, ICMCB, UMR 5026, F 33600 Pessac, France
‡International Advanced Energy Science Research and Education Center (IAESREC), Graduate School of Energy Science, Kyoto University, Yoshida-Honmachi, Kyoto, Japan
§Laboratoire de Chimie et de Physique Approche Multi-échelles des Milieux Complexes (LCP-A2MC), Institut de Chimie Physique et Matériaux (ICPM), METZ cedex 3, France
¶Institute of Molecular Sciences, UMR 5255, CNRS, Université de Bordeaux, Talence, France

Chirality is a property of asymmetry resulting, for an object, from the non-superposition of its image in a mirror. The notion of symmetry breaking, inherent in the organization of matter, the formation of new structural edifices, and, more fundamentally, weak interactions, is

omnipresent. From the physics of elementary particles to molecules of the living world and functional organisms, to climatic phenomena inducing vortices of forces, chirality often plays a crucial role. It is also a conception of geometry exploited in design fields and man-made constructions for its functionality and uniqueness.

In this chapter, we will focus on the chirality observed in solid state matter, that is, chirality based on the solid state organization of atoms or molecules. While there can be an important overlap with inorganic chiral nanostructures or nanoparticles for which there are a number of reviews, the solid state matters treated in this chapter can include crystals as well as amorphous solids of both organic and inorganic molecules. As we will discuss below, the study of the chirality of solid materials has mainly been focused on asymmetric ordered and periodic structures. When atoms are considered as a repeating unit, chiral crystals of achiral molecules can be classified as 3D asymmetric periodic structures. Chiral crystal faces of centric crystals and chiral 2D patterns of achiral molecules can be classified as 2D asymmetric periodic structures. Individual helical polymeric chains, chiral carbon nanotubes, and nanoparticles can be classified as 1D asymmetric periodic structures. We should also mention that chiral quasicrystals do not have mirror symmetry or translational symmetry, but have rotational symmetry, showing beautiful chiral ordered structures. We will also describe how chirality can be enhanced by the 2D or 3D organization of building components of solid materials. We will close with a discussion of spectroscopic methods to characterize chiral objects and assemblies.

1.1 Genesis of Chirality in 3D Bulk Materials*

Chiral purification of molecules is a major preoccupation in many fields of natural sciences, ranging from origin of life studies [1], to chemistry, physics, and pharmacy [2]. Today, most newly approved chiral pharmaceuticals are marketed as single enantiomers [3], and thus, the need to produce enantiopure molecules is an important challenge for industry [4–6]. Three main approaches include the transformation of chiral natural products,

* Sections 1.1.1 and 1.1.5 were adapted from the thesis of the late Angela Valentin-Perez, University of Bordeaux, 2019.

asymmetric synthesis, and resolution of racemates. The resolution of racemates has proven to be the most economical and straightforward approach, and resolution via crystallization remains a technique of major industrial importance [7–9]. Solid state resolutions can be accomplished by: (i) preferential crystallization, where an initial enrichment may promote a full chiral discrimination in the solid state. In some cases, the crystallization of the preferred enantiomer in a conglomerate system is industrially feasible. (ii) the addition of chiral adducts for the formation and selective crystallization of diastereomers. However, these strategies most often have a maximum yield of 50% of the desired enantiomer. Nevertheless, recent work in solid state deracemization, where a racemic mixture is transformed entirely into a single chirality [10], poses promising perspectives in the production of chiral species with excellent atom economy.

In this section, we will briefly present different methods of resolution and deracemization via crystallization, with a focus on historical milestones.

1.1.1 History

Foundational studies, notably by French physicists, paved the way for the discovery of molecular chirality by L. Pasteur in 1848. In 1808 É.-L.Malus discovered plane-polarized light, light that propagates through a given media with its electric and magnetic field vectors in-phase along the propagation direction [11]. In 1811, F. Arago discovered optical rotation, defined as the rotation of the plane of polarization that occurs when polarized light passes through an optically active substance [10]. In 1817, J.-B. Biot found that some natural compounds, such as sucrose, oil of turpentine, camphor, and tartaric acid, rotated polarized light in solution, in the liquid state or in the vapor phase [12]. Finally, in 1824, A.-J. Fresnel discovered circularly polarized light (CP light) and that optical rotation is due to the different refractive indices for left and right CP light [13]. CP light can be defined as light that propagates through a given media with its electric and magnetic field vectors perfectly out-of-phase along the propagation direction.

In 1844, Biot presented a communication by M. Mitscherlich to the French Academy of Sciences commenting that tartrate rotated polarized light, while paratartrate had no such effect, even if the two molecules otherwise had identical physical properties [14]. The breakthrough

regarding the relationship between the two substances came with Pasteur's realization that the crystal forms of optically active sodium ammonium tartrate tetrahydrate and the corresponding salt of paratartrate — now known to be a racemic mixture of D- and L-tartrate — were not identical. After careful examination, Pasteur noted that sodium ammonium paratartrate crystallizes as a mixture of two hemihedral crystals with different hemihedrism directions (Figure 1) [15]. In this way, the two crystals were nonsuperimposable mirror-images (enantiomorphous). Using tweezers, Pasteur manually separated the two types of crystals and measured their optical activity in solution, finding that the two solutions rotated light in the opposite direction, but with the same absolute intensity. In this manner, he demonstrated the relationship between crystal form and physical properties, although the structure of the tartrate molecules at that time was unknown.

Soon thereafter, Pasteur hypothesized that the molecular natures of the tartrates must be different. This led to the proposition that the molecules share the same relationship with each other as the crystals do, that is they are identical, but nonsuperimposable forms [16]. He named one form "right tartaric acid" and the other "left tartaric acid," and expressly related them to differences in their three-dimensional structure. Paratartaric acid was also known as *racemic* acid at the time, and thus the term *racemic* mixture, or racemate, was adopted for equimolar compositions of two

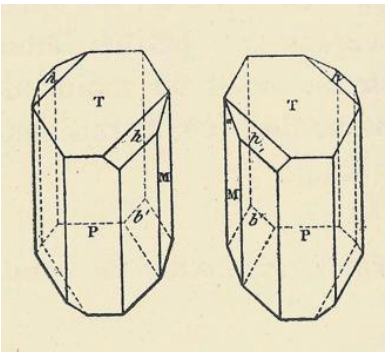

Figure 1. Pasteur's drawing of the crystals of sodium ammonium paratartrate [L. Pasteur; C. R. Acad. Sci. Paris, 1848, 26, 535.]

enantiomers. Crucially, the discovery of molecular chirality can be attributed to the propensity of the paratartrate enantiomers to segregate during crystallization to form a mechanical mixture of enantiomorphic crystals, called a conglomerate.

Conglomerate crystallization also played an important role in the discovery of biological homochirality. In 1851, Pasteur studied the crystals of the naturally occurring amino acid L-asparagine and identified their chiral crystal habit [17]. In 1885, Italian chemist A. Piutti obtained a new form of asparagine by the slow evaporation of the mother liquor from a large-scale synthesis of L-asparagine [18]. He manually separated the crystals of the new species from those of L-asparagine and found that the two crystal habits were enantiomorphous. In addition, the optical rotation of the new compound was found to be equal in absolute magnitude and opposite in direction to that of natural asparagine, while the chemical properties and elemental composition were identical. At that moment, Piutti put forth two hypotheses: that the new substance was either a stereoisomer or a geometric isomer, with the amino group in another position with respect to the natural asparagine. Therefore, Piutti designed a synthetic pathway which allowed him to demonstrate that L-asparagine has the amino group in the α position with respect to the carboxylic acid, and also to establish that his newly isolated form was the mirror image isomer of natural asparagine [19]. Furthermore, he realized that D-asparagine had an intensely sweet taste while the L-form was tasteless [20]. This was the first example of a difference in taste found for enantiomerically related substances and, as anticipated, the first example of enantioselectivity at a biological receptor. This important milestone stimulated additional studies in this area that established the importance of interactions between chiral substances and biological systems. Nowadays it is known that biological systems are also chiral, presenting, for example, amino acids in the L-form or carbohydrates in the D-form.

1.1.2 Conglomerate Crystallization

Pasteur's discovery of molecular chirality can be attributed to considerable good luck. Sodium ammonium tartrate tetrahydrate crystallizes as a conglomerate mixture of hemihedral crystals only below 27°C. At higher

temperatures, the two enantiomers crystallize together in centrosymmetric crystals. Had the room in which Pasteur was working been warmer, the discovery of molecular chirality would certainly have been delayed. It was shown by H. W. B. Rooseboom in 1899 that racemic mixtures can crystallize in three principal forms [21]. Most commonly, they crystallize as racemic, centrosymmetric crystals containing both enantiomers in a periodic array (Figure 2). This preponderance of racemic crystals has been attributed by O. Wallach to a denser, and thus more energetically stable, packing in heterochiral crystals [22]. While "Wallach's Rule" has been supported by many studies [23], there also exist numerous exceptions [24].

The formation of conglomerates has been estimated to occur in less than 10% of racemic mixtures [24, 25], although theoretical calculations suggest that the prevalence of conglomerates is likely approximately twice higher [26]. The rarest example is when both enantiomers are present, but randomly distributed throughout the crystal, forming a total or partial solid solution [27]. The crystallization behavior of racemic mixtures is usefully described by phase diagrams, either binary for a pair of optical isomers, or ternary for the pair of isomers and an optically inactive solvent [12]. Many of these diagrams have been verified experimentally, and we refer readers to excellent reviews on the subject [12, 28].

In general, it is not possible to predict the solid state outcome of a racemic mixture, although conglomerates appear to be favored in salts [29], and are highly dependent on the nature of the anion in cationic coordination compounds [30]. As we will see shortly, the presence of

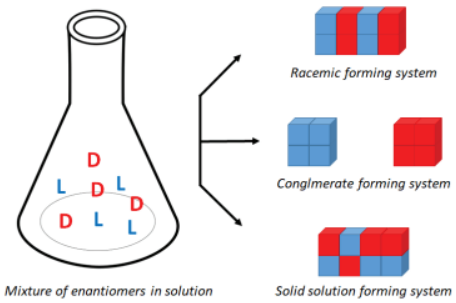

Figure 2. Different outcomes of crystallization of racemic mixtures of enantiomers.

conglomerate crystallization is useful for resolution and deracemization processes, and the rapid identification of conglomerate-producing systems is of great interest. As chiral compounds can only crystallize in one of 65 space groups, known as Sohncke groups [31], conglomerates are often capable of second harmonic generation (SHG). The screening for SHG in a recrystallized racemic mixture is thus a suitable method to determine whether the system crystallizes as a conglomerate or a racemic compound [32]. When conglomerates are not available for the desired compounds, the synthesis of conglomerate co-crystals can alleviate this problem. An early example was the observation that tri-*o*-thymotide crystallizes as a racemate from methanol, but as a conglomerate as the hexane, benzene, or chloroform solvate [33]. Methods for crystal structure library [34] or phase diagram [35] screening in the prediction of co-crystals have been reported.

The examples of enantiomorphism in the solid state discussed above are due to the intrinsic chirality of the molecule, for example, the presence of stereogenic carbon atoms. However, enantiomorphism can also arise from a dissymmetric arrangement of achiral molecules in the crystal packing. Such compounds are thus completely optically inactive in the liquid or solution state, but their crystallization leads to optically active crystals. The most common examples are sodium chlorate and quartz. The β-phase of quartz crystallizes in space group $P6_422$ or $P6_222$, depending on the handedness of the supramolecular arrangement around the 6-fold axis, while the low-temperature form of α-quartz crystallizes in either space group $P3_221$ or $P3_121$ depending on the arrangement around the 3-fold axis [36]. In sodium chlorate, it is an opposite rotation around a 2_1 screw axis that provides the two crystal enantiomorphs [37]. In a similar fashion, chiral polymers can arise from achiral monomers [38]; this topic will be discussed in detail in a following section of this chapter.

While an enantiopure molecule must crystallize entirely in either right-handed or left-handed crystals, there is no thermodynamic reason why quartz or sodium chlorate should prefer one enantiomorph over the other. Thus the average distribution of several crystallizations should tend toward 50:50 of both enantiomorphic crystals. While it had been shown that a collection of $NaClO_3$ crystals, when ground into a powder, was optically inactive, in 1898 F. Kipping and W. Pope demonstrated that the

number of crystals of each handedness converged with increasing crystal population [39]. Since then, several studies on conglomerate formation of sodium chlorate have been performed, in part due to its crystallization in a cubic crystal system as large, transparent crystals. These features allow $NaClO_3$ and related compounds, such as $NaBrO_3$, to be studied by polarized optical microscopy, without interference from linear optical effects. While Pasteur was able to visually separate crystalline enantiomers, this kind of manual triage is nontrivial, as the crystals must present clear hemihedral faces. Methods to preferentially crystallize one or the other enantiomer would render this separation step unnecessary.

1.1.3 Preferential Crystallization

The presence of conglomerate crystallization opens several pathways to enrich the enantiomeric excess in the solid state [28b, 28d]. In 1866, D. Gernez, a student of Pasteur, accomplished a selective crystallization of sodium ammonium tartrate tetrahydrate by seeding a supersaturated solution of the racemic mixture with an enantiopure crystal. If a right-handed crystal was used, right-handed tartrate was crystallized, and likewise for the left-handed enantiomer [40]. Seeding of racemic mixtures with enantiopure crystals, also called entrainment or preferential crystallization (PC), is now a common way of obtaining enantiomerically enriched material [28d, 41], and has been notably used in the industrial preparation of chloramphenicol, L-dopa, and (−)-menthol [42]. This process typically requires several cycles, where the crystallization of one enantiomorph leads to an excess of the other enantiomorph in solution, which is then precipitated using the appropriate seed, and so on [43]. As this as an arduous process, refinements have made PC more efficient for industrial applications [28b, 28c, 44]. We bring the interested reader's attention to two recently published reviews on PC [45].

In the case of solution-stable enantiomers, the theoretical maximum yield cannot exceed 50%. To increase the yield of the desired enantiomer, racemization in solution can be provoked, sometimes referred to as second-order asymmetric transformation [46]. During the crystallization of one enantiomer, its antipode is in excess in solution and converts to the desired enantiomer, and thus the yield can approach 100% enantiomeric

excess in the solid state. Because the racemization in solution removes any excess of the undesired enantiomer, the probability of the nucleation of the counter-enantiomer decreases and this process can be carried out at lower supersaturation levels than classical PC. This is particularly interesting for industrial applications [47], and the discovery of racemization agents is an active field of study [48]. The transformation of a racemic mixture to one single enantiomer is called deracemization, and is distinct from the resolution techniques described above.

1.1.4 Deracemization

Deracemization refers to the transformation of a chirally undifferentiated medium to a single enantiomer in 100% yield. Different deracemization methods have been established, using chiral catalysts, often enzymes [49], with the application of photochemical [50] or redox [51] perturbations. This is a vast subject and, as it is not necessarily dependent on crystallization, it will not be treated here. In 1954, E. Havinga laid out the three required conditions for deracemization via crystallization to occur: (i) no racemic crystal formation, (ii) the substance must be racemized in solution, and (iii) crystal growth must be faster than the formation of crystal nuclei [52]. In an article entitled "Spontaneous Formation of Optically Active Substances," Havinga demonstrated this phenomenon using the chiral ammonium salt methyl-ethyl-anilinium iodide, which spontaneously crystallized from supersaturated solutions in sealed tubes. This phenomenon is based on the fact that the free energy of a conglomerate suspension will decrease with decreasing surface area of the crystal. Therefore, the Ostwald ripening process, the production of large crystals at the expense of small ones that dissolve, will eventually lead to the production of a single enantiopure crystal [53]. While this process is very slow, it can be hastened by grinding [54], temperature cycling [55], exposure to ultrasound [56], pressure [57], or microwaves [58].

A century after Kipping and Pope showed that unstirred sodium chlorate solutions give rise to an equal distribution of both enantiomorphs, D. Kondepudi and coworkers demonstrated that an enantiomeric excess could be obtained when the crystallization took place while stirring [59]. Each crystallization is stochastic, such that prevailing enantiomer is

randomly obtained. The theory was put forth that the chirality of the first appearing crystal (by primary nucleation), the "mother crystal," seeds the chirality of the subsequent "daughter" crystals (by secondary nucleation) [60]. Stirring allows a cleaving of the mother crystal to generate secondary nucleation sites, which then reduces the concentration of the solution such that the formation of additional mother crystals via primary nucleation is suppressed.

C. Viedma later refined this theory by showing that extremely rapid primary nucleation of $NaClO_3$ in a highly oversaturated solution also results in symmetry breaking, with no need of a single mother crystal [61]. Later he showed that stirring a conglomerate of $NaClO_3$ suspended in water in the presence of glass beads also results in a 100% ee of one or the other enantiomorph. This was attributed to the equilibrium between solid and solution phases, such that the smallest crystallites dissolve, thus favoring the handedness of the larger crystals, eventually leading to complete symmetry breaking over several dissolution/recrystallization cycles. This process is now called Viedma ripening [54] and is an important method in the deracemizations of chiral organic compounds (in the presence of a racemizing agent) [62], as well as other conglomerate-forming systems [63]. Different mathematical models taking into account the influence of crystal growth, attrition and secondary nucleation have been proposed [64]. A general schematic for Viedma ripening is shown in Figure 3.

Another related deracemization technique that relies on racemization in solution and auto-amplification of small enantiomeric excesses in the solid phase is temperature cycling induced deracemization (TCID),

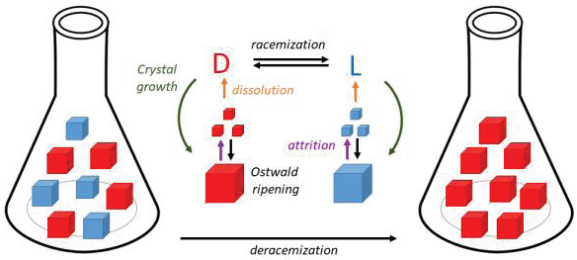

Figure 3. General scheme for deracemization processes by crystallization of conglomerates.

discovered by G. Coquerel in 2013 [24b, 64d]. In TCID, starting from a suspension of mirror-imaged crystals in equilibrium with their common saturated solution in which both enantiomers interconvert freely, the thermal energy applied to the suspension in a (quasi-)steady state produces dissolution/crystallization cycles, and the racemic mixture is progressively converted into an enantiopure material [8, 48a, 65]. This process has been modeled computationally taking into account various parameters such as crystal size distribution, secondary nucleation, agglomeration, crystal growth, dissolution, and racemization processes [66], although the exact mechanism of this process is still unknown. Recently, a method of combining deracemization of the medicine praziquantel with temperature cycling and conglomerate crystallization under flow conditions has been reported [67] and scale-ups of the TCID process have been accomplished [68].

The previously discussed deracemization techniques do not require the addition of any chiral auxiliary, but the final chirality of the crystalline product cannot be controlled. In order to select the desired enantiomer, the addition of small quantities of non-co-crystallizing chiral substances or the use of chiral solvents can bias the reaction [69]. It was shown as early as 1898 that adding a chiral carboxylate to the crystallization of achiral $NaClO_3$ resulted in a preference for one crystalline enantiomorph over the other [39]. Chiral impurities in the environment have been suspected in some cases of favoring *d*-$NaClO_3$ [70] when no exogenous auxiliary is added. This kind of preference for one crystal handedness has been found to be due to differential interactions at the crystal surface which can inhibit crystal growth or promote nucleation [71]. Another approach is the addition of a stoichiometric quantity of a chiral additive, which preferentially interacts with one enantiomer, resulting in the formation of crystalline diastereomers. This resolution technique will be discussed in the following section on Pasteurian resoluton, with an emphasis on chiral anions.

1.1.5 Pasteurian Resolution

Pasteurian resolution is a method to obtain enantiomerically pure molecules from racemic mixtures via the formation and selective crystallization of diastereomeric salts. With different physico-chemical properties between diastereomers, particularly solubility, they can be separated by a selective

crystallization step and there is no need for conglomerate formation [72]. This method was first applied by Pasteur in 1853 in the separation of a racemic mixture of tartaric acid [73]. The addition of derivatives of natural chiral bases quinotoxin and cinchotoxin allowed the crystallization of the right and left tartrates, respectively, while the other enantiomer remained in solution.

The resolution of amino acid derivatives by this method was first described by E. Fischer in 1899, using brucine and strychnine [74]. Pasteurian resolution continues to be broadly applied in industry for organic systems using chiral acids or bases from the chiral pool of natural products [75]. Basic resolving agents include the widely used α-methylbenzylamine and quinine, cinchonine, cinchonidine, ephedrine, morphine, strychnine, brucine, etc. [25, 42, 76]. Acidic resolving agents for racemic bases include mainly tartaric acid and derivatives, as well as mandelic acid [77], L-malic acid [78], 2-naphthylglycolic acid, (*S*)-phenylpropionic acid, and camphorsulfonic acid and derivatives [42, 76b].

The conjugate bases of such acidic resolving agents have also been used for the resolution of chiral coordination compounds. The first such resolution was performed in 1911 by V. L. King, a student of A. Werner, who resolved cis-$[Co(en)_2(NH_3)Cl]^{2+}$ with 3-bromocamphor-9-sulfonate [79]. As coordination complexes are most often cationic, a series of natural and synthetic anions have been developed for their crystalline resolution. In order to have efficient ion pairing, the chiral anions need to fulfill the following conditions, as enumerated by J. Lacour and coworkers [80]:

1) The stereogenic element(s) should be close to the charged complex to favor enantioselective ion-pairing interactions.
2) The anion should be chemically and configurationally stable.
3) The chiral anions should be easily accessible by synthetic procedures and, if possible, in an asymmetric manner.

The earliest examples of chiral anions employed for enantiomeric resolution of coordination compounds are the conjugate bases of natural chiral carboxylic and sulfonic acids, such as tartaric, mandelic, or 10-camphorsulfonic acids (Figure 4) [81]. Nevertheless, these anions possess a rather large number of potential conformations. To obtain a

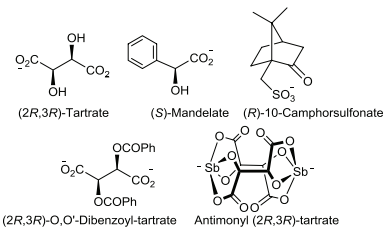

Figure 4. Examples of chiral anions obtained from natural chiral carboxylic and sulfonic acids.

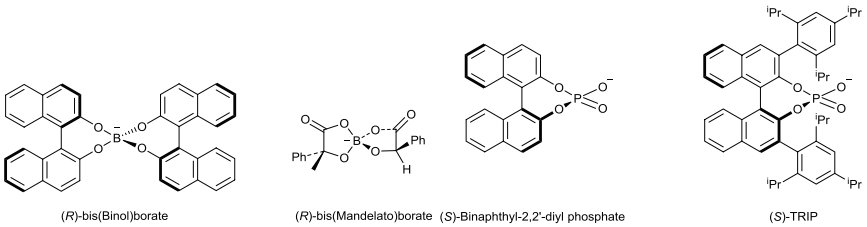

Figure 5. Examples of chiral borate anions and chiral derivatives of phosphoric acid.

more rigid structure, they can be coordinated to metal ions, yielding an anionic complex. The most well-known example is the antimonyl (2*R*,3*R*)-tartrate anion (Figure 4), commercially available as the potassium salt, which has been extensively used for chiral resolution in coordination chemistry [82].

Chiral borate anions can also be synthesized by employing chiral ligands. H. Yamamoto and coworkers first synthesized this type of anion (Figure 5), employing [1,1′]-binaphthalenyl-2,2′-diol (popularly known as BINOL) as the ligand [83]. Chiral resolutions using sodium salts of the (*R*)- or (*S*)-bis(mandelato)borate anion were reported by I. Williams and coworkers for the separation of the enantiomers of the alkaloid tetrahydropalmatine, 1,2-diaminopropane, and the complex $[Co(phen)_3]^{3+}$ (phen = 1,10-phenanthroline) [84].

Conjugate bases of phosphoric acid derivatives frequently provide chiral anions. For many years, the (*S*)-(+)- or (*R*)-(–)-binaphthyl-2,2′-diyl phosphate (Figure 5), which presents planar chirality, was the only such anion used in asymmetric anion-mediated processes [85]. Nowadays,

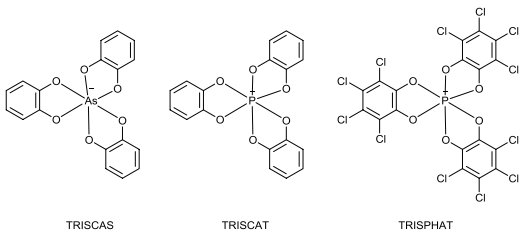

Figure 6. Examples of chiral octahedral anionic complexes of P(V) and As(V).

there are many derivatives of this phosphate with substitution at the 3,3′-positions. One example is the so-called TRIP anion (Figure 5), synthesized by B. List and coworkers, which is characterized by the presence of very large 2,4,6-triisopropylphenyl substituents at the binaphtyl 3,3′-positions [86]. The resolution of the enantiomers of a dicopper(I) molecular trefoil with binaphthyl-2,2′-diyl phosphate was reported by J.-P. Sauvage and colleagues in 1996 [87].

Octahedral anionic complexes of hexacoordinated phosphorus and arsenic atoms, presenting helicoidal chirality are also often employed to perform chiral resolutions. These compounds are synthesized as racemates using achiral ligands, and are typically resolved using chiral alkaloids [88]. The TRISCAS (tris(catecholato)arsenate(V)), TRISCAT (tris(catecholato)phosphate(V), and TRISPHAT (tris(tetrachloro-1,2-benzenediolato)phosphate(V) anions are of particular importance (Figure 6). TRISCAS was synthesized for the first time in 1919 by R. Weinland and J. Heinzler [89], and the complex was resolved into its optical enantiomers by A. Rosenheim and W. Plato in 1925, who proposed the tris-chelate structure of the anion [88c], which was confirmed by single-crystal X-ray diffraction in 1972 [90]. It has been employed for the chiral resolution of asymmetric boron cations [91] and helicate dimer and trimer copper (I) complexes [92]. The X-ray crystal structure of the racemic triethylammonium salt of TRISCAT was published in 1973 [93], but its resolution was not performed until 1979. Nonetheless, the resolved anion racemizes rather quickly in solution depending on the nature of the solvent and acidity of the medium [94] For this reason, it is not a very useful chiral anion to perform enantiomeric resolution, but these racemization problems are solved in its perchlorinated TRISPHAT monoanion derivative. Its X-ray

crystal structure was reported for the diethylammonium salt in 1992 [95], and its chiral resolution was managed in 1998 by Lacour *et al*. [88b]. This anion has been used, for example, as a resolving agent of M(II) complexes with ligands based on bipyridine and phenanthroline [96].

1.1.6 Helical Conformations of Achiral Polymers in Solids

In the previous section, we discussed the rich variety of crystalline arrangements of chiral molecules. Dissymmetric arrangement of achiral units, such as atoms, can also be the origin of enantiomorphism in solid crystals [39, 97]. As previously mentioned, and shown in Figure 7a and c, helical arrangements of atoms are found in both crystals of α-quartz [98] and sodium chlorate [99]. Similar dissymmetry can also be found in the helical conformation of achiral polymers. In 1954, C.W. Bunn and E.R. Howells first revealed the helical structure of polytetrafluoroethylene (PTFE) in the solid crystal by X-ray diffraction studies (Figure 7b) [100].

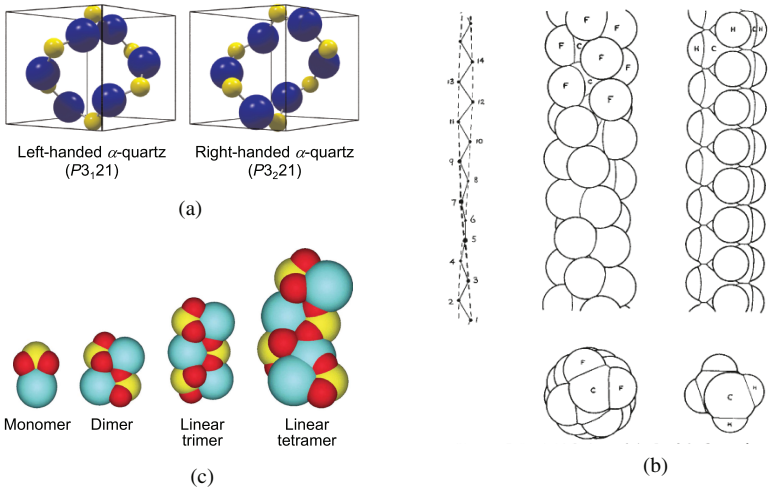

Figure 7. (a) Crystal structures of left- ($P3_121$ space group) and right-handed ($P3_221$ space group) α-quartz. O atoms: large blue, Si atoms: small yellow. (b) Left: twisted zigzag chain found in fluorocarbons. Center: fluorocarbon molecule (side and end views). Right: hydrocarbon molecule. (c) Isotactic oligomerization of sodium chlorate. (a) Adapted with permission from Ref. [98]. (b) Reprinted with permission from Ref. [5, 100]. (c) Adapted with permission from Ref. [99].

After this report, detailed structures of PTFE crystals have been studied by various analytical techniques such as X-ray crystal structural analysis, thermal analysis, and computer simulation, leading to the discovery of the 13/6 helical conformation in the phase II and the 15/7 helical conformation in the phase II and IV [101]. From a historical standpoint, it is interesting to note that the helical conformation of PTFE was reported in the same decade as the right-handed α-helix of polypeptides [102], the right-handed double-stranded helix of DNA [103], and the helical conformation of isotactic polypropylene in the crystal state [104]. The most thermodynamically stable conformation of hydrocarbon chains is the flat zigzag (all *trans*) conformation. However, in the case of fluorocarbons, this zigzag conformation of the polymer chain is twisted. This was attributed to steric hindrance due to the larger van der Waals diameter of the fluorine atom (2.70 Å), compared the hydrogen atom (2.40 Å), whereas the span of the zigzag (distance between the carbon with its next neighbor carbon) is 2.54 Å. Similarly, numerous isotactic vinyl polymers having a helical conformation in the solid crystal have been reported [105].

In such structures, even though steric hindrance forces helical conformations, there is no preference for the helical handedness (left-handed or right-handed) taken by such polymers unless they have chiral sources (chiral center, chiral axis, chiral plane, etc.). When the energy barrier for helix inversion is relatively low, switching between the left- and right-handed helical conformations is a dynamic process in solution and they remain as a racemic mixture [106]. R.J.M. Nolte *et al*. synthesized poly(*tert*-butyl isocyanide) having a high helix inversion barrier in solution and succeed in the enantiomeric separation of synthetic helical polymers by chiral chromatography in 1974 [107]. Meanwhile, Y. Okamoto and coworkers succeeded to synthesize a one-handed helical conformation of isotactic poly(triphenylmethyl methacrylate) by using chiral catalysts [108]. Indeed, the formation of the helical polymer chain is attributed to the ensemble of intramolecular factors (internal rotation potentials around the single bond, repulsions and van der Waals interactions between nonbonded atoms, electrostatic interactions, hydrogen bonds, etc.), and intermolecular factors (hydrogen bonds, intermolecular interactions in the crystal lattice, etc.). A number of helical polymers having well-designed molecular structures have been reported [109] and the strategies have been

expanded to various research fields including chiral supramolecular polymers [110]. Carbon nanotubes might also be thought of as achiral unit-based helical polymers, as carbon atoms or benzene rings are considered as the repeating units. A single-walled carbon nanotube (SWCNT) can be considered as a cylinder rolled up from a graphene monolayer with a chiral vector $\mathbf{C_h} = n\mathbf{a_1} + m\mathbf{a_2} \equiv (n, m)$, where $\mathbf{a_1}$ and $\mathbf{a_2}$ are unit vectors and (n, m) defines the chirality (or helicity) of the SWCNT. Left- and right-handed SWCNTs show negative and positive values of $n - m$, respectively [111]. Chiral SWCNTs have been obtained both by chirality-controlled growth methods and solution-based separation approaches.

Such helical polymers, dispersed in solvents, can be deposited on substrates by methods such as drop casting [112], spin coating [113], and spray coating [114] giving access to homochiral solid materials (Figure 8a).

It is also possible to synthesize helical polymers with a selected handedness by use of an external inducer, and to simultaneously solidify them in order to arrest the helicity inversion dynamics (Figure 8b). K. Akagi *et al*. reported the synthesis of helical polyacetylene by using a chiral nematic liquid crystal as a chiral reaction field [115] in which the handedness of helical polyacetylene can be controlled by the chirality of the liquid crystal. The dihedral angle between the repeating units (-CH=CH-) of helical polyacetylene ranged from 0.02° to 0.23°. This very small

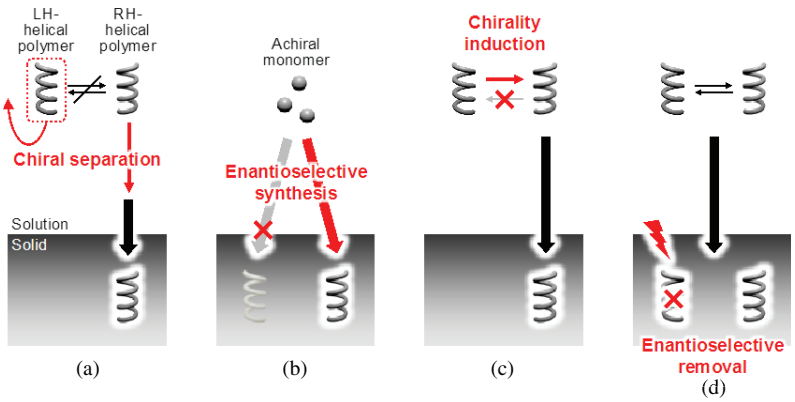

Figure 8. Various preparation approaches of chiral solid materials from helical polymers. (a) Chiral separation, (b) enantioselective synthesis, (c) chirality induction, and (d) enantioselective removal.

dihedral angle maintains the planarity of π-conjugated polymer chain with a high *trans* content (90%) resulting in high electron conductivity, and to form one-handed helical structures with a nonzero dihedral angle [116].

Instead of using chiral liquid crystals, CP light can be used to synthesize enantiopure polymers. M. Iwamoto *et al*. reported that chiral polydiacetylene (PDA) films were produced by using ultra-violet CP light for photopolymerization [117]. In this case, CP light was used as the only chiral source without any chiral molecules in the system, and the sign of the circular dichroism (CD) signals of the obtained PDA films was dependent on the selection of left- and right-handed CP light irradiation. S.-T. Wu and coworkers applied this technique to enantioselective synthesis of chiral coordination polymers [118]. They synthesized [{Cu(succinate)(4,4′-bipyridine)}$_n$]·4H_2O_n having left- and right-handed helical structures by irradiation of left- and right-handed CP light in the visible range, respectively.

Some researchers took another approach in order to create chiral polymer solids from an achiral polymer solution taking advantage of its dynamic helix inversion behavior in solution (Figure 8c). For example, the formation of solid films from achiral polymers with chiral dopants can give access to stable chiral structures having memory effects.

E. Yashima *et al*. reported that only one helical handedness of charged poly(phenylacetylene) derivatives can be induced by small chiral guest molecules, and can be memorized in a film by the *Layer-by-Layer (LbL)* assembly technique [119]. R.B. Kaner *et al*. prepared the optically active polyaniline/N-methylpyrrolidinone (NMP) solution by doping with *S*- or *R*-camphorsulfonic acid (CSA). Subsequently, optically active thin films of *R*- or *S*-camphorsulfonic acid (CSA)-doped polyaniline were prepared by casting on a glass plate. The obtained film retained its optical activity after removal of CSA. Interestingly, this optically active polyaniline thin film showed enantioselective discrimination of D- and L-phenylalanine, as confirmed by a visible color change [120]. G. Guerra *et al*. reported the induced circular dichroism (ICD) from the δ-form of syndiotactic polystyrene (s-PS), obtained by evaporation from chiral volatile solvents such as limonene and carvone, even after removal of these chiral compounds [121]. The helical conformation of δ-s-PS memorized by co-crystallization with chiral molecules shows high thermal stability up to 240°C. The

imprinted chiral nano-space, which the chiral molecules occupied during the co-crystallization process, can be used for chirality induction in achiral chromophore guests such as azulene [122]. A number of examples of chirality induction by co-crystallization with chiral compounds are summarized in review articles [123].

CP light can be also used as an external force for chirality induction [124]. G. Iftime and coworkers observed ICD signals from an initially achiral azobenzene liquid crystalline polymer in the solid state after irradiation with CP light [125]. The sign of the ICD can be switched by selecting the handedness of irradiated CP light. Induction of a preferred-handed helical conformation of π-conjugated polymers, such as poly(9,9-dioctylfluorene-2,7-diyl) (PDOF) and its derivatives, has been well studied by the groups of Nakano [126] and Fujiki [127].

Finally, enantioselective removal of helical polymers from racemic solids might also be included in the key methods for preparing enantiopure helical polymer-based-solid materials (Figure 8d). M. Teraguchi *et al*. reported the helix-sense-selective photodegradation of a racemic poly[4-dodecyloxy-3,5-bis(hydroxymethyl)phenylacetylene] (poly(DoDHPA)) membrane by irradiation of single-handed with CP light (Figure 8d) [128].

1.1.7 Generation of Chirality in Amorphous Solids

As discussed above, the study of the chirality of solid materials has mainly been focused on asymmetric ordered and periodic structures. When atoms are considered as a repeating unit, chiral crystals of achiral molecules can be classified as 3D asymmetric periodic structures (Figure 9b). Chiral crystal faces of centric crystals and chiral 2D patterns of achiral molecules can be classified as 2D asymmetric periodic structures (Figure 9c). Individual helical polymers, chiral carbon nanotubes, and nanoparticles can be classified as 1D asymmetric periodic structures (Figure 9d). We should also mention that chiral quasicrystals do not have mirror symmetry or translational symmetry, but have rotational symmetry, showing beautiful chiral ordered structures (Figure 9e and f).

On the other hand, noncrystalline (non-ordered and nonperiodic structures) materials also have the potential to show chiral properties.

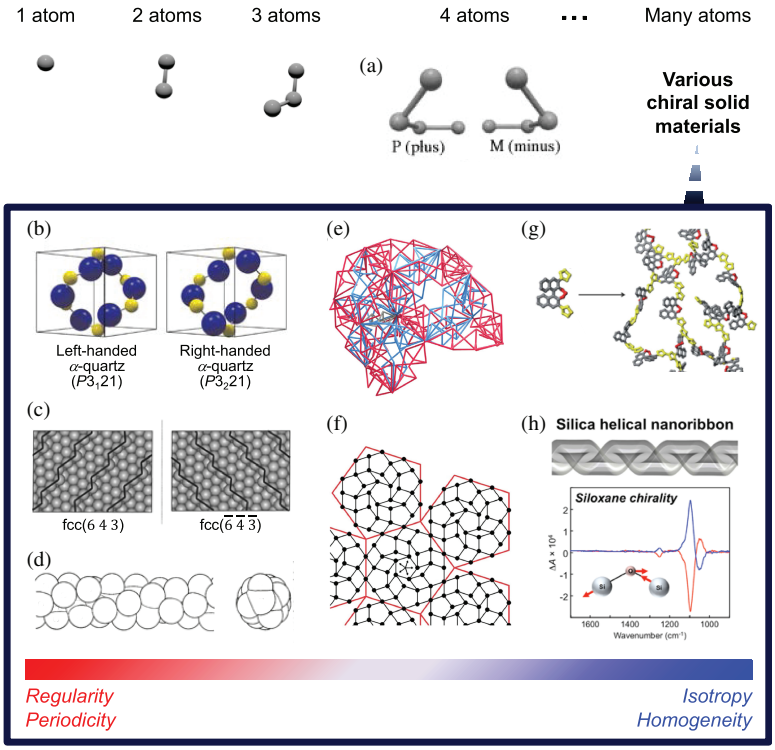

Figure 9. Generation of chirality from the arrangement of atoms in solid materials. (a) Arrangements of four atoms having plus (left) and minus (right) torsion angles. (b) 3D asymmetric periodic structure found in the crystal structure of quartz. (c) 2D asymmetric periodic structure found in the ball models of fcc(643) and fcc($\bar{6}4\bar{3}$) surfaces. (d) 1D asymmetric periodic structure found in the fluorocarbons. (e) Chiral 3D icosahedral quasicrystalline structure. (f) The dodecahedron 2D network decorated with the chiral pentagonal quasilattice. (g) Locally chiral and globally isotropic 3D structure found in the microporous BINOL-based polymer network. (h) Schematic illustration of amorphous silica helical nanoribbon (top) and its VCD signals at Si-O-Si asymmetric stretching vibrational band (bottom). (a) Adapted with permission from Ref. [129]. (b) Adapted with permission from Ref. [98]. (c) Adapted with permission from Ref. [138]. (d) Adapted with permission from Ref. [5, 100]. (e) Adapted with permission from Ref. [139]. (f) Adapted with permission from Ref. [140]. (g) Adapted with permission from Ref. [133]. (h) Adapted with permission from Ref. [136].

Considering atoms as the smallest unit, the simplest element of molecular chirality is the torsion angle θ ($-180° < \theta < 180°$) made from four atoms as shown in Figure 9a) [129]. Note that even one atom [130], monoatomic cations [131], and monoatomic anions [132] can show induced chirality

under the support of chiral inducer, such as chiral molecules and chiral molecular assemblies, constructed from more than four atoms. C. Bleschke *et al*. synthesized enantiopure microporous 1,1′-bi-2-naphthol (BINOL)-based polymer networks (Figure 9g) [133], and the obtained microporous polymer material showed high enantioselectivity as a heterogeneous organocatalyst. The interesting point is that this material has local chirality and global isotropy (homogeneity). Similar examples can be easily found in the solution phase, but only a few examples have been reported in solid systems. A good example is that of amorphous (noncrystalline) chiral metal oxides synthesized by the sol-gel condensation of metal alkoxide in the presence of chiral organic molecules as templates. This approach was first reported by Shinkai *et al*. [134]. After this report, numerous helical (morphologically chiral) silica nano-materials have been synthesized and been studied for their chiroptical properties [135]. Interestingly, in some cases, the obtained helical (or twisted) nano silicates show strong vibrational circular dichroism (VCD) signals at Si-O-Si asymmetric stretching vibrational band even after removal of organics by calcination (Figure 9h) [136]. XRD and nano beam electron diffraction results confirmed that the obtained helical (and twisted) nano silica materials are amorphous (noncrystalline). These results indicate that the silica helices have a local chiral arrangement of Si and O atoms, similar as shown in Figure 9a, but also a globally isotropic siloxane network. The lack of regularity, including periodicity and translational symmetry, provides global isotropy (homogeneity) [137]. Such a viewpoint might lead to further developments in the field of chiral solid materials.

1.2 Generation of Chiral Surfaces

1.2.1 Chiral Metal Surfaces for Enantioselective Recognition

As it is well known, a wide variety of substances have their own stereoisomers, such as pharmaceuticals, nutraceuticals, and agricultural chemicals. In an achiral environment, enantiomers of chiral compounds generally exhibit similar physical and chemical properties [141]. However, when they interact with other chiral compounds or chiral surfaces, the enantiomers often exhibit different biological and pharmacological responses [142], and many pharmaceutical products and agrochemicals

must be enantiopure to be effective [143]. It is important to realize that more than 50% of the drugs currently in pharmaceutical use have at least one chiral center in their structures and most of the top-selling drugs in the market are used in their enantiopure form [144]. Perhaps the most dramatic example indicating the importance of enantiopure compounds in the pharmaceutical industry is the case of thalidomide, widely used in the 1960s by pregnant women as a sedative and to relieve morning sickness [145]. Whereas the D-enantiomer is harmless, with desirable tranquilizing properties, its L-enantiomer is teratogenic and leads to malformations in embryos.

Therefore, the separation of racemic molecules is of substantial significance not only in basic sciences but also for technical applications, such as fine chemicals and drug development. However, precisely because of the similarity of their physical and chemical properties, their resolution in an achiral environment remains a challenge [141, 146]. Many single-enantiomer drugs are obtained either by separation methods, often involving chromatographic columns [147], or via asymmetric catalysis, which ideally should be performed heterogeneously to minimize problems associated with solubility and with the purification of the products [148]. Both of those methods involve chemistry on solid surfaces. Resolution methods based on the recognition or separation of enantiomers remain an attractive choice to obtain enantiopure compounds.

The most commonly used resolution method is chiral chromatography [147] capable of enantioselective recognition. Other efficient techniques include crystal resolution (as discussed previously), liquid–liquid extraction, and membrane separation which are also used for separation or preparation purposes [149]. Each of these methods has its unique capabilities for enantiomeric recognition, separation, or quantification.

1.2.2 Chirality on Solid Crystal Surfaces

Chiral solid surfaces represent highly useful environments for a variety of heterogeneous enantioselective processes to produce enantiopure bioactive compounds [146c, 150]. Indeed, there are many inherently chiral inorganic materials, such as chiral metal surfaces, which have demonstrated a wide variety of enantiospecific properties and enantiospecific

interactions with chiral adsorbates [151]. The design of various types of chiral surfaces using single-crystal Cu surfaces has been extensively studied in recent years with the aim of identifying materials having surfaces with optimal enantiospecific interactions with the chiral compounds of interest [152]. Such surfaces can have potential applications in analytical chemistry, chiroptical measurements, chemical, and electrochemical synthesis as well as separation.

1.2.2.1 *Chirality of crystal surfaces due to crystal structure*

The surface of acentric (without a center of symmetry) crystals is chiral. Among numerous chiral crystals including over 210 acentric crystals of metal oxides [153], natural quartz, which is known to be the most abundant chiral oxides, has been often used for the investigation of chiral surfaces (Figure 10a and b). For example, powders of enantiomorphic quartz show enantioselective adsorption of various chiral compounds such as metal complexes [154] and amino acids [155]. However, it was pointed out that: (1) different crystallographic planes of quartz show different absorption behaviors including non-enantioselective absorption [150b, 156]. Therefore, potentially strong enantioselective absorption effects on some of the crystallographic planes might be weakened or even disappear by the mixing of different crystallographic planes resulting from the powdering process, and (2) most natural quartz crystals are internally twinned by inversion [150b]. Therefore, powdering natural crystals will necessarily blend both left- and right-handed domains [150b]. Therefore, it is crucial that a single crystallographic plane of quartz is used for studying enantioselective adsorption.

Achiral crystals having a symmetrical structure, such as face-centered cubic (fcc), body-centered cubic (bcc), or hexagonal close-packed (hcp) structures (figure 10d) can provide chiral surfaces when their surfaces lack mirror symmetry (known as a chiral kink, chiral step (figure 10e), or chiral terrasse (figure 10f)) [157]. For example, A.M. Cody and R. D. Cody reported that gypsum ($CaSO_4 \cdot 2H_2O$) shows strong asymmetric crystal growth in the presence of various chiral molecules [158]. C.A. Orme *et al*. reported a similar asymmetric crystal growth phenomenon of the centric crystal of calcite ($CaCO_3$) (figure 10c) in close interaction with

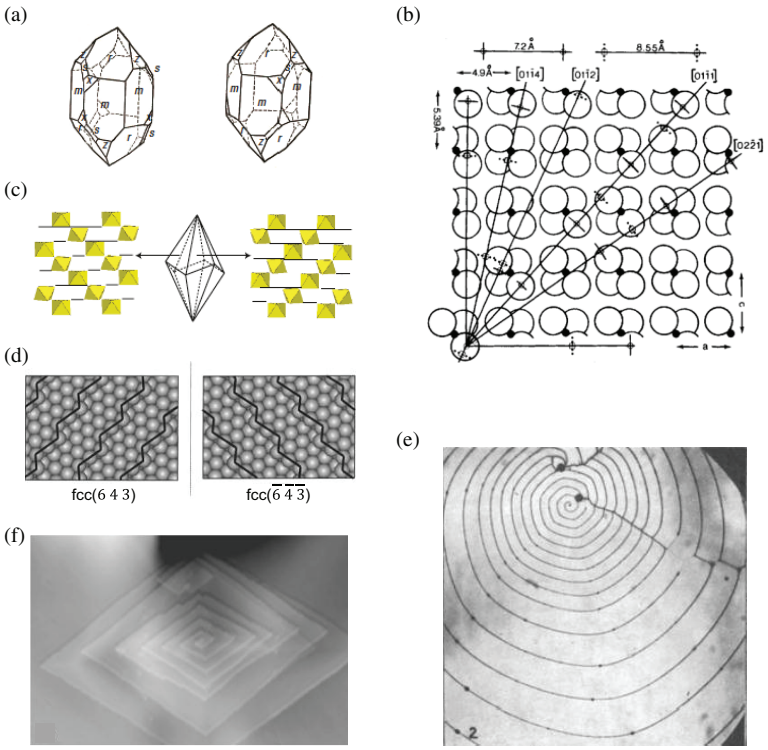

Figure 10. Chirality on crystalline solid surfaces. (a) Left- and right-handed variants of quartz crystals. (b) The $(10\bar{1}1)$ crystal face of L-quartz. (c) The common $\{21\bar{3}1\}$ trigonal scalenohedral (dogtooth) form of calcite (center). features adjacent crystal faces with enantiomorphic surface structures. The markedly acentric surface structures of both the (3121) face (left) and the (2131) face (right) consist of corner-linked chains of CaO_6 octahedra, cross-linked by planar CO_3 groups, which are seen almost on edge. L-aspartic acid is observed to adsorb preferentially on the (3121) face, whereas D-aspartic acid adsorbs preferentially on the (2131) face. (d) Ball models of fcc(643) and fcc$(\bar{6}\bar{4}\bar{3})$ surfaces. (e) Spiral-patterned step on the crystal surface of carborundum (SiC). (f) AFM image of a spiral terrace of a polyethylene single-crystal. (a and c) Reprinted with permission from Ref. [150b]. (b) Reprinted with permission from Ref. [155b]. (d) Adapted with permission from Ref. [138]. (e) Reprinted with permission from Ref. [163]. (f) Adapted with permission from Ref. [162b]

amino acids [159]. Such mirror symmetry-broken (chiral) surfaces of centric calcite show enantioselective adsorption depending on the exposed facet [160]. Similar chiral surfaces of various materials, including metals [138, 161], polymers [162], and other inorganics [163], have also been

studied. The study of chiral surfaces and their enantioselective behavior has been carried out by various analytical techniques such as scanning tunneling microscopy (STM), atomic force microscopy (AFM), low-energy electron diffraction (LEED) [161a, 164], SHG [165], electrochemical methods [166], the quartz crystal microbalance (QCM) method [167], density functional theory (DFT) calculations, and others.

The introduction of chirality on achiral metal surfaces can be achieved by adsorption both of chiral and achiral molecules [168]. The transformation of the surface nature of metals or metal oxides in order to bring in chiral features can be achieved when they are in interaction with chiral or achiral molecules (organized chirally) which then create the chiral environment.

1.2.2.2 *Adsorption of chiral molecules on solid surfaces*

It has been shown that enantiopure chiral adsorbates can develop several ordered structures on various chiral and achiral surfaces, the structures of which depend on the coverage of the adsorbates and the temperature [169]. This reflects a delicate balance among different driving forces, such as intermolecular interactions, which often include hydrogen bonds, and bonds with surface functions [170]. For example, at low surface coverage, many homochiral adsorbates tend to agglomerate to form small, well-defined supramolecular aggregates consisting of a few molecules (monomers, dimers, trimers, and tetramers) in short linear structures. The majority of the molecules are found in dimers [171], while at high coverage, these homochiral adsorbates are found with tetrameric and pentameric units, sometimes with reduced symmetry due to the formation of linear chains, herringbone patterns, or other supramolecular arrangements (Figure 11) [168c, 172].

When using a racemic mixture of chiral absorbates in solution, either they can form racemates from the pairing of enantiomers [173], especially if the two enantiomers strongly interact with each other, or they can show phase separation into homochiral domains (conglomerates) [174]. In general, the formation of homochiral conglomerates on surfaces results from the self-assembly of small homochiral cluster units. These homochiral clusters have higher stability than the corresponding heterochiral clusters,

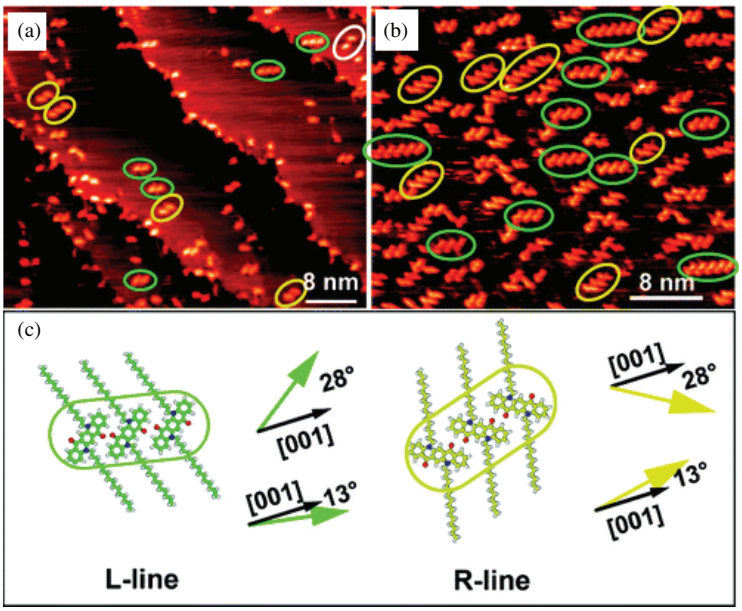

Figure 11. Adsorption of a prochiral quinacridone derivative (QA16C) with two alkyl chains of 16 carbon atoms on a Cu(110) surface: (a and b) STM images obtained at 150 K on Cu(110) at low (QA16C) coverages. One-dimensional structures of QA16C with different orientations are observed. Monomers, dimers, trimers, tetramers, and pentamers are identified. (c) Schematic representation of backbone and line orientations. (a) $U_{bias} = -1.07$ V, and $I_t = 0.50$ nA. (b) $U_{bias} = -1.29$ V, and $I_t = 0.08$ nA. Adapted from Ref. [171] with permission, Copyright 2010 American Society.

leading to conglomerate formation. Using DFT calculations, it was revealed that the small clusters can be obtained by strong hydrogen bonding, while the larger, racemic supramolecular arrangements appear to be controlled by weaker van der Waals interactions. The initial small homochiral clusters disappear with increasing surface coverage. The formation of well-defined aggregates and self-assembled patterns on the material surface determines the degree of enantiosegregation of the final monolayers made with racemic mixtures of molecules. A few cases where homochiral and heterochiral structures of the same molecule are formed on the surface have also been reported [173b], possibly resulting from a balance between intermolecular interactions mediated by hydrogen bonds and the

strength of adsorbate-surface bonds. Thus, the final structures that form on the surface are the result of a subtle balance between several competing forces of similar magnitude.

Chirality can also be generated by the absorption of achiral or prochiral molecules on achiral surfaces. R.A. Wolkow *et al*. observed chirally adsorbed *trans*-2-butene, which is prochiral molecule, on the achiral silicon(100) surface (Figure 12a) [175]. Similar phenomena were found in the absorption of glycine molecules on the Cu(100) surface [176] and 4-trans-2-(pyrid-4-yl-vinyl) benzoic acid (PVBA) on Pd(110) [177]. Meanwhile, Q. Chen and N.V. Richardson reported an example of surface chirality generation by the adsorption of 1D molecular aggregates. When adenine is adsorbed on a Cu(110) surface with a low coverage at room temperature and annealed at 370 K, the molecules form dimer-based short chain-like aggregates aligned ±19.5° from the [100] symmetry direction of the Cu(110) surface (Figure 12b and c) [178]. T.G. Gopakumar reported that Ni-tetramethyl-tetraazaannulene (Ni-TMTAA), which is an achiral and non-prochiral molecule, forms right- (*R*-form) or left-handed (*S*-form) propeller-shaped chiral trimers to produce well-patterned homochiral 2D surface motifs on the Au(111) surface [179]. In the case of prochiral 1-nitronaphthalene (NN), the deposition of NN in the range of 0.05–0.2 monolayers (ML, 1 ML corresponds to a close-packed molecular layer) on the Au(111) surface leads to chiral (C_2 symmetric) decamer formation (Figure 12d) [180]. The handedness of such chiral decamers is determined by a combination of high-resolution STM observation and local-density calculations. They concluded that chiral clusters are stabilized by intermolecular hydrogen bonding between the O atom of the NO_2 group and the H atom of the naphthalene moiety. The idea of adsorption of prochiral molecular assemblies can be expanded to 2D chiral packing. C.B. France and B.A. Parkinson reported the 2D chiral packing domain of naphtho[2,3-a]pyrene (NP) on the Au(111) surface (Figure 12e) [181]. Even when adsorbent molecules are highly symmetric and achiral (non-prochiral), surface chirality can also be generated by forming chiral patterns from them. For example, M. Neuber and F. Schneider *et al*. reported that achiral (D_{6h} symmetric) benzene molecules form a chiral 2D pattern when adsorbed on an Rh(111) surface (Figure 12f) [164a]. Many similar examples, such as adsorption of C_{2h} symmetric anthracene derivatives on a

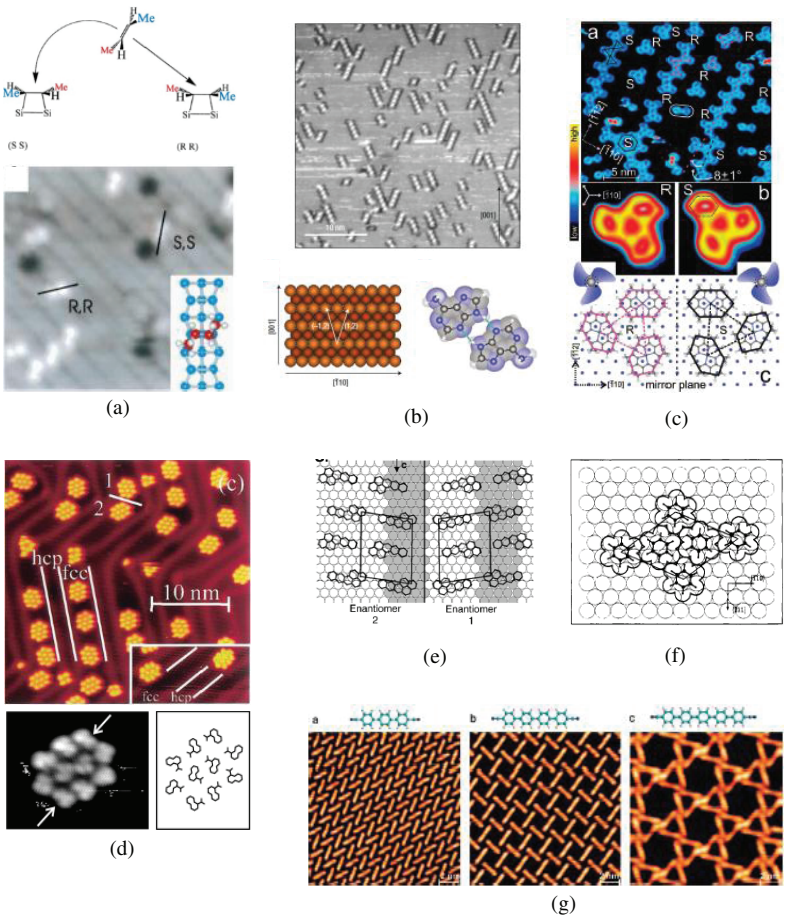

Figure 12. Generation of surface chirality by adsorption of achiral molecules on achiral crystalline solid surfaces. (a) Top: Two distinct faces of planar trans-2-butene. Bottom: STM image of trans-2-butene on a Si(100) surface. (b) STM image of adenine chains on a Cu(110) surface. (c) Top: STM image of Ni-TMTAA on Au(111). Middle: Pseudo-three-dimensional presentation of a constant-current STM image of R and S trimers of Ni-TMTAA. Bottom: Sketch of R (magenta) and S (black) trimers of Ni-TMTAA. (d) STM image of an Au(111) surface with adsorbed 1-nitronaphthalene (NN). Magnified STM image of the NN decamer (bottom left) and its theoretical modeling (bottom right). (e) 2D chiral packing model of naphtho[2,3-a]pyrene (NP) on a Au(111) surface. (f) Proposed chiral structure of densely packed benzene molecules adsorbed on an Rh(111) surface. (g) STM images of various 2D chiral patterns formed by a dicarbonitrile triphenyl molecule (left), a dicarbonitrile tetraphenyl molecule (center), and a dicarbonitrile pentaphenyl molecule (right) on an Ag(111) surface. (a) Reprinted with permission from Ref. [175]. (b and c) Reprinted with permission from Ref. [178a]. (d) Reprinted with permission from Ref. [180b]. (e) Reprinted with permission from Ref. [181]. (f) Reprinted with permission from Ref. [164a]. (g) Reprinted with permission from Ref. [183].

graphite surface [182] and D_{2h} symmetric dicarbonitrile-polyphenyl molecules on an Ag(111) surface (Figure 12g) [183] have been reported. In such cases, the formation of these homochiral domains of achiral/prochiral molecules on achiral surfaces occurs with the same probabilities.

S.M. Barlow and R. Raval suggested that surface-induced chiral systems of achiral or prochiral molecules can be classified into two categories: (1) adsorption-induced chiral motifs (point chirality of individual molecules) and (2) adsorption-induced chirally ordered domains (organizational chirality) [184]. There are 10 crystallographic 2D point groups, compare to the 32 crystallographic 3D point groups. Among which, 5 chiral 2D point groups are permitted. In the case of organizationally chiral systems, among 17 possible 2D space groups compared to the 230 crystallographic 3D space groups, 5 of these 2D space groups are chiral [164b]. Therefore, the selection of various adsorbing molecules, solid materials, and crystal faces of solid surface may provide a diversity of chiral surfaces.

1.2.2.3 *Grafting of chiral molecules onto a metal surface*

Chirality can be imparted to achiral surfaces by covalently grafting chiral modifiers [185]. When a chiral molecule interacts strongly with an achiral flat metal surface the interaction could in principle lead to a reconstruction of the metal surface. In general, the binding of adsorbates will induce a restructuring of the surface only if the gain in the adsorption energy of the molecule on the disrupted surface, compared to adsorption on the non-restructured surface, overcompensates the energy required to break the metal bonds. On oxides, chiral molecules can bind with reactive sites on the surface, typically with terminal hydroxo groups. This approach has been widely used for the development of stationary phases of enantioselective chromatography columns [147, 186], as well as for anchoring biomaterials such as RNA strands, enzymes, and proteins, on surfaces in order to develop biosensors, bioassays, and nanoparticle carriers [187]. Furthermore, this approach has also been widely used to create chiral catalysts by immobilizing homogeneous chiral catalysts on solid oxide surfaces [188] in order to design reusable heterogeneous catalysts. In some cases, immobilized catalysts may exhibit higher enantioselectivity than their free counterparts [188b]. If the molecule used as a chiral

modifier is complex enough, it is possible that it creates a chiral environment where the reactant can anchor and be chemically converted enantioselectively [138, 166a, 166c].

1.2.2.4 *Molecular imprinting by using chiral molecules as templates*

To encode chiral information in metals, imprinting with chiral molecules as the template is one of the most promising strategies to create and retain chiral structures or chirally imprinted cavities inside bulk metals even after removal of the templates [189]. It is well known that there is a dynamic relationship between the atomistic structure of a metal surface and molecules adsorbed on that surface [190]. Adsorbates can induce a variety of structural changes on the surfaces of metallic substrates. When the adsorbate is chiral, the atoms on the surface of metal substrate can be restructured to give chiral surfaces. This is the essence of chiral imprinting; transmission of molecular chirality to the structure of a metal surface [191].

One can imagine that once a chiral imprinting agent has induced surface reconstruction, it could, in principle, be removed from the surface, leaving an intrinsically chiral and clean metal surface giving access to the new chiral or prochiral adsorbates to directly interact with it. However, in most of the observed cases of chiral imprinting, the organic imprinting agent remains adsorbed on the imprinted metal surface limiting the direct contact of other adsorbing species with the intrinsically chiral metal surface and, in this regard, the imprinted surface is similar to that of a chirally modified achiral metal surface. The chirality of the metal surface under the adsorbed chiral imprinting agent could still amplify the enantiospecific interactions of chiral adsorbates with the imprinted surface [191a]. Therefore, one of the interesting challenges of chiral imprinting as a means of preparing intrinsically chiral materials is the displacement of chiral imprinting agents, while keeping the chiral nature of the surface, which is a difficult task. Indeed, the interaction between the surface and the adsorbate can be quite strong. One possible method to remove the chiral adsorbate could be by thermal decomposition. However, this usually brings contamination onto the surface. In addition, heating of the imprinted metal surface typically results in lifting or loss of the chiral reconstruction to regenerate its originally achiral

structure. The ideal process for removal of a chiral imprinting agent would be to leave the surface in its chirally imprinted, high-Miller-index state without contamination. This probably requires a low-temperature process. For example, exposure of the imprinted surface to an adsorbate with a heat (energy) of adsorption that is greater than that of the chiral imprinting reagent could displace the imprinting reagent into the gas phase [151b, 151c]. The ideal displacing adsorbate after the replacement of the imprinting agent should then have a weak barrier to decomposition into fragments, which will readily desorb from the surface.

Another approach to imprint chiral information on a metal surface is based on the chemical reduction of a metal-ligand complex in order to create organic-doped metals. For example, hybrid metal/organic imprinted materials have been successfully prepared at room temperature using chemical reduction in the presence of the organic molecules which serve as templates while entrapped within the metal matrix [192]. Several chiral metal structures have been obtained in this way [193], retaining the chiral information even after removal of the template [189, 194]. Mesoporous core-shell Pd@Pt bimetallic nanoparticles have also been successfully synthesized by the chemical reduction approach. The resulting materials exhibit a very high specific surface area with no aggregation problem, as is often the case with metal nanoparticles, as well as a high potential for the enantioselective recognition of the corresponding chiral compounds [195]. Chirally encoded cavities on metals and metal oxides have been successfully generated in CuO films deposited onto several achiral metal surfaces, for example, Au(001) and Cu(111), by using tartrate enantiomers as chiral templates [196]. The stereochemical information is maintained in the CuO film even after the removal of the chiral molecules. It was found that CuO films imprinted with (+)-tartaric acid and (–)-tartaric acid show opposite configurations, having a $(1\bar{1}\bar{1})$ orientation with an enantiomeric excess of 95% in the first case, and the latter one exhibiting a $(\bar{1}11)$ orientation with an enantiomeric excess of 93% [196a].

It has been shown that the combination of encoding molecular structures and mesoporous features has distinct advantages, such as a significantly improved enantioselectivity due to an extremely high active surface [195]. This new concept has been successfully applied to various types of chiral imprinted cavities using several chiral template molecules.

1.3 Chiral Nanocrystals and Nanoparticles

In the previous sections, we have looked at the generation and expression of chirality in 3D bulk materials and on the solid surfaces. Here, we will discuss how chirality can be induced in semiconductor or metallic nanocrystals. This approach has attracted a lot of attention due to the excellent physical and chemical properties of the nano-objects. There are various ways to obtain chiral signals from nanocrystals (NCs) or nanoparticles (NPs). C. Gautier and T. Burgi [197] have described three categories of chiral metal NPs: (a) chiral ligands are used to stabilize the NPs creating a chiral "footprint" on the surface of the metal, (b) the optical activity arises from an intrinsically chiral inorganic core shape, and (c) the inorganic core can be achiral and the optical activity is induced by a chiral environment such as a chiral organic shell or chiral electrostatic field. This classification is based on the chiral source of the chiral optical activity: particle structure, environment, and surface, respectively.

This classification was further developed by N.A. Kotov *et al*. [198] in an extensive review describing four types of chemical and physical origins of chirality for NPs based on differences in the formation process: (a) NPs with a chiral surface of the inorganic core, which is normally induced through adsorption of chiral molecules, (b) NPs with a chiral pattern of the surface ligands, (c) the inorganic core of metal of the NP has chiral shape itself, and (d) polarization effects in the inorganic core, which can be induced by chiral molecules or assembly of NPs.

In this section, we will specifically focus on the chirality of NPs induced by chiral ligands or lattices and chirality induced by the chiral shape of individual particle. We will discuss the hierarchical organization of particles in the next section

1.3.1 Chirality Induced by Chiral Ligands

Chiral ligands have been used to endow chirality to nanocrystals of noble metal such as Au nanoclusters [199] and Ag NPs [200]. In 2005 [201], a pair of gold nanocluster enantiomers was first reported. The gold nanoclusters capped with S- or R-penicillamine show mirror image CD spectra, and their dissymmetry g-factors decreased with increasing gold

nanocluster size. The mechanism of chirality induction by chiral ligands is supposed to involve chiral footprints or a local chiral distortion of the surface atoms. In order to have a better understanding of the chirality induction, the binding model between chiral ligands and Au NPs has been studied using infrared (IR) and VCD spectroscopy [202]. Thiols and carboxylic acid groups were shown to co-interact with the gold particle leading to the chiral footprint, which is the origin of the observed optical activity.

Semiconductor nanocrystals such as quantum dots (QDs) with chiral ligands also attract a lot of attention due to their excellent absorption and emission properties. In 2007 [203], Gun'ko first reported optically active CdS (QDs) combined with S- or R-penicillamine. Many subsequent reports can be found on the investigation of the mechanism of chirality induction from chiral ligands to QDs. In 2009 [204], Nakashima *et al*. reported the observation of CD signals from CdS, CdSe, or CdTe QDs capped with D- or L-cysteinemethylester hydrochloride. Interestingly, neither CdSe nor CdTe QDs showed CD signals in the range of the first exciton peak (CdSe at 470 nm and CdTe at 540 nm). This indicates that the observed CD signals cannot be attributed to the first excitonic transition in QDs cores but rather to the surface Cd atoms coordinated by the ligands S atoms, and thus the chirality of QDs is supposed to originate from the distorted Cd-S-ligands surface. Furthermore, the chirality of the nanocrystals (NC) surface was maintained even after chiral ligands were exchanged with an achiral thiol, providing a chiral memory effect (Figure 13a).

In 2015 [205], Gun'ko proposed that CdSe/ZnS-based QDs have intrinsic chirality caused by the presence of natural chiral defects, even when they are prepared without using chiral ligands. As shown in Figure 13b, the TEM images of as-prepared QDs show the possible presence of left- and right-handed screw dislocations. The QDs are supposed to form racemic mixtures of left- and right-handed QDs and also non-chiral QDs. They have shown that the racemic mixture of such nanocrystals can be separated using water-soluble chiral ligands mixed with oil-soluble QDs through phase transfer methods.

In 2016 [206], Balaz found that the CD signals could be inversed only by an alteration of the chiral ligand structure. The QDs combined with two

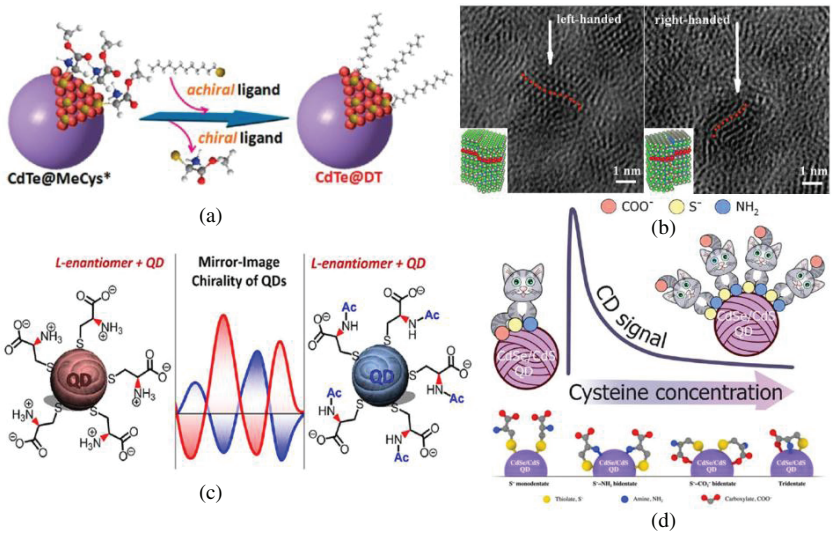

Figure 13. (a) Schematic of the chiral memory effect by ligand-exchange reactions from chiral ligands D- or L-cysteinemethylester hydrochloride (MeCys) to 1-dodecanethiol (DT). (b) TEM images of the CdSe/ZnS QDs. The arrows indicate possible screw dislocations and the red dotted lines indicate the direction of the dislocations. The insert pictures indicate the atomistic models of CdSe/ZnS QDs with right and left screw dislocations, where the dislocations are set in the (010) plane of the CdSe core of nanocrystals with (–) Burgers vector and (+) Burger vector. (c) Same configuration but different binding arrangements of N-acetyl-L-cysteine and L-homocysteine-QDs resulting in mirror CD images. (d) The strong influence of the concentration of a chiral amino acid (cysteine) on its binding modes upon the surface of CdSe/CdS QDs, resulting in varying chiroptical activity and corresponding CD signals.

only slightly different ligands both having the same configuration (L-acetylcysteine vs L-cysteine) configurations show mirror CD images (Figure 13c). It was demonstrated that the CD signals are determined not only by the absolute configuration but also by the binding modes between the chiral ligands and the QD surface.

An inversion of CD signals of HgS QDs upon heating was reported with N-acetyl-L-cysteine [207]. This inversion was explained by Fourier transform infrared (FTIR) spectroscopy and theoretical calculations as being the result of the modification of the coordination between chiral ligands and the surface of the QDs upon heating. Gun'ko *et al*. [208] then reported that the binding mode of cysteine on CdSe/CdS QDs strongly

depends on the concentration of the ligands (Figure 13d). With lower cysteine concentrations, the cysteine coordinated to the QD surface in a tridentate mode with enhanced CD signals, while, at higher cysteine concentrations, the tridentate coordination mode changed to a bidentate coordination mode, resulting in a decrease in the CD signals. Indeed, the chiral ligands have a big influence on the chirality induction process.

Beyond the chirality induction based on chiral ligands, the inherent structural properties of nanocrystals such as their size, shape, and crystal structure also show an impact on chirality induction. In 2011, Tang [209] and Markovich [210] reported simultaneously that CdSe QDs combined with chiral ligands show optical activity, which depends on the QD size. As shown in Figure 14d, the dissymmetry g-factor decreased with increasing QD size, which is likely due to the decreasing surface-to-volume ratio. In 2017 [211], Tang reported that CdSe rods with different aspect ratios having L/D-cysteine ligands show the shape dependence of the g-factor, which increases with increasing aspect ratio (sphere to rod), reaching a saturation value with an aspect ratio at about 3.7, based on theoretical calculations. Recently, CdSe/CdS with various morphologies such as quantum rods, nanoflowers, tadpoles, and tetrapods, have also been reported [212]. In 2018 [213], Tang reported that the CdSe nano-platelets having wurtzite (hexagonal) and zincblende (cubic) crystal structures showed different behaviors in terms of chirality induction from their L/D-cysteine ligands. CdSe nano-platelets (NPLs) with a hexagonal crystal structure showed 10 times higher CD spectra compared to those having a cubic crystal structure. This was explained as arising from their different dipole moments and polarization.

In general, bare core QDs suffer lower photoluminescence quantum yield (PLQY) due to their surface traps. QDs with core-shell structure like a CdSe core and a CdS shell could boost the PLQY, which could be widely used in lighting and displays. QDs with a CdSe/CdS core-shell structure showed g-factors and PLQYs which depended on the CdS shell thickness; PLQY increased with CdS shell thickness, while the g-factor decreased due to the increased distance between chiral ligands and CdSe core (Figure 14d) [214].

Recently, perovskite nanocrystals with chiral ligands have been reported to show promising CD and CPL properties [215]. The best

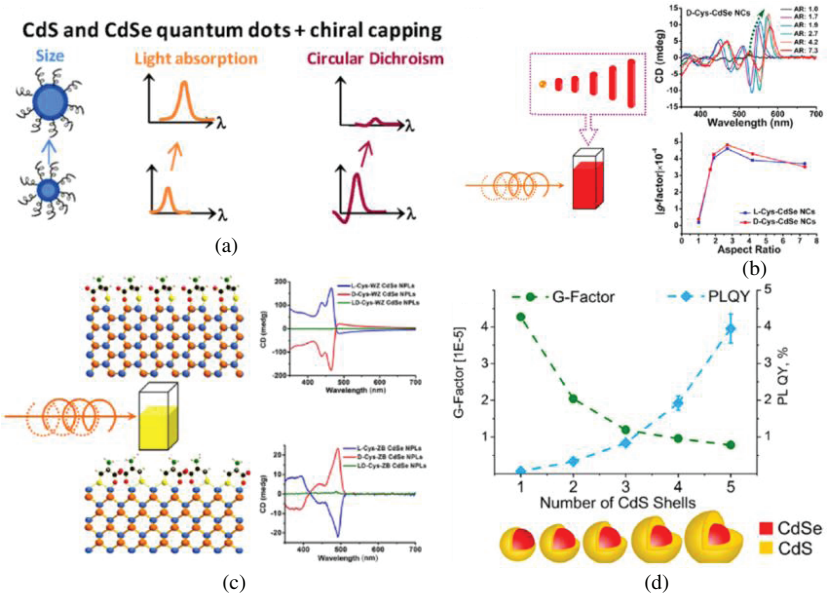

Figure 14. (a) Size effect of the optical activity of CdSe and CdS QDs induced by chiral ligands. The increasing size of QDs results in stronger, red-shifted absorption but lower CD signals. (b) Shape effect of the optical activity of CdSe quantum rods induced by chiral ligands. The dissymmetric g-factor increases with the aspect ratio before reaching a plateau. (c) Crystal structure effect of the optical activity of CdSe nano-platelets (NPLs). The hexagonal crystal structured CdSe NPLs capped with L- or D-cysteine ligands show a distinct CD shape and a much stronger CD signal compared with cubic crystal structured CdSe NPLs. (d) Shell-thickness effect of the optical activity of CdSe/CdS core-shell structured QDs induced by chiral ligands. The increased shell thickness results in enhanced fluorescence but lower induced dissymmetric g-factor.

dissymmetry g-factor approaches 0.02, which is among the highest in the nanoparticle/chiral ligand system.

1.3.2 Chiral Shape of Inorganic Materials

Chiral biomineralized structures in Nature represent an inexhaustible source of inspiration showing hierarchical organization from the nanoscale to the macroscale. Beautiful examples like snail shells, the narwhal tusk, or coccoliths can be observed. Interestingly, the connection between the

largely homochiral biomolecules and the larger-scale assemblies and biomineral structures remains largely unknown [216]. A number of studies on bio-inspired minerals or inorganic materials with chiral shapes have been published in the last 20 years, including SiO_2 [217], TiO_2 [218], ZnO [219], CdS [220], Ag [221] films, CuO nanoflowers [222], or glutamic acid [159, 223]. Jiang *et al* have shown that chiral, hierarchically organized architectures for calcium carbonate can be controlled simply by adding aspartic acid. Toroidal suprastructures having a "right-handed" spiral morphology are induced by L-Asp and a "left-handed" morphology is induced by D-Asp. The proposed growth mechanism is based on the tilting of the NPLs due to their binding with chiral amino acids: cooperative tilting of the ensemble of the NPs (or nano-platelets NPLs), amplified over several length scales, creates oriented mineral platelets and chiral vaterite suprastructures (Figure 15) [224].

The structural complexity of such chiral materials has recently been studied with model systems like gold-cysteine platelets. The use of polydisperse platelets has shown that the evolution of multiparticle systems depends on particle symmetry and asymmetry more than on size. Such studies open a pathway to a large family of chiral colloids with complex architectures and chiroptical and chemical properties [224].

In 2014 [225], tellurium and selenium NPs having chiral shapes were synthesized, assisted by chiral thiolated biomolecules, with ECD

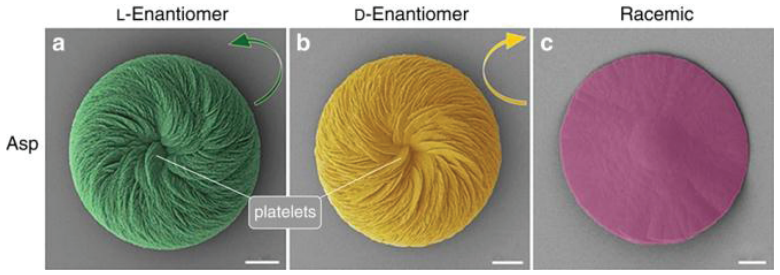

Figure 15. SEM images of calcium carbonate (vaterite) toroids grown in 20 mM L- or D-aspartic acid (a and b, respectively) or in a racemic mixture (c). The L-enantiomer produces right-handed chiral toroids (green), the D-enantiomer left-handed toroids (yellow), and the racemic mixture non-chiral platelets (purple). Scale bars are 6 μm (a and b) and 8 μm (c). Adapted with permission from [224].

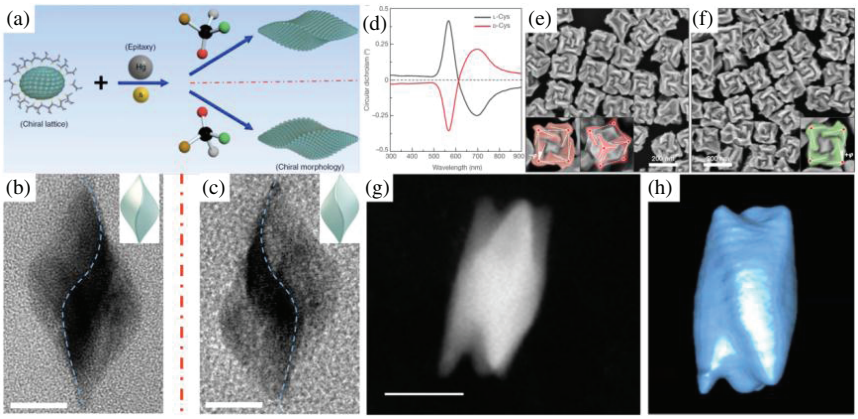

Figure 16. (a) Schematic of the growth process based on the epitaxial principle with involvement of chiral molecules to tailor the morphology chirality. (b) and (c) Typical TEM images of prevailing individual twisted triangular bipyramid nanostructures. Blue-dashed curves are added to guide the eyes for different twisting orientations in the chiral nanostructure. Scale bar, 20 nm. Inset pictures indicate the structural models of two mirrored nanostructures. (d) Circular dichroism spectra of chiral NPLs synthesized using L-cysteine (black) and D-cysteine (red). (e) SEM image of L-cysteine Au NPs. The highlighting in the insets illustrates the fact that the edges (solid lines) are tilted by an angle ϕ with respect to the vertices (red dots) and cubic outline (dashed lines), as viewed along the [110] (left) and [111] (right) directions. (f) SEM image of D-cysteine Au NPs. The inset highlights the tilted edges (solid lines), cubic outline (dashed lines), and tilt angle ($+\phi$). (g) Dark-field STEM image and (h) tomographic reconstruction of the tellurium particle. Scale bar, 100 nm.

dissymmetry g-factors up to 0.03. Figure 16g and h shows the dark-field STEM images and tomographic reconstruction of the tellurium particle, respectively. The chiral tellurium nanostructures were transformed into chiral gold and silver telluride nanostructures with g-factors up to 0.015. In 2017 [226], chiral HgS nanocrystals were synthesized using chiral ligands. Starting from achiral α-HgS nanocrystals as seeds, the successive ion layer adsorption and reaction (SILAR) method was applied for epitaxial growth of HgS, which lead to twisted bipyramid nanocrystals. The prevailing morphology from epitaxial growth is determined by the chiral molecules utilized and is independent of the crystallographic chirality of the seed NPs. Figure 16b and c shows the right- and left-handed twisted bipyramid

nanostructures with D- or L-penicillamine molecules as chiral morphology modifiers during the epitaxial growth process, respectively. In 2018 [227], chiral gold NPs, which showed strong optical activity with a large dissymmetry g-factor of 0.2, were synthesized by using chiral amino acids and peptides to control the handedness. As shown in Figure 16d, L- and D-cysteine were used to synthesize right- and left-handed helicoid cubes, which showed mirror CD images. Figure 16e and f shows the SEM images of right-handed and left-handed helicoid cubes, respectively. A number of reports on chiral gold NPs followed [228], and the chiral morphology of palladium NPs was obtained by the same protocol [229].

Inorganic nanocrystals having chiral shape exhibit promising potential applications due to the large g-factors of their CD signals. Designing fluorescent nanocrystals having a chiral shape represents a new challenge with extremely promising applications.

1.4 Chiral Hierarchical Organization of Nanostructures

1.4.1 Organization of Achiral Objects

Organized ensembles of nanostructures can show collective and often enhanced properties, which are different from those displayed by individuals or mixtures of disorganized samples in the bulk. Therefore, the preparation of controlled aligned/organized NPs or molecular assemblies has been the subject of increasing research efforts [230].

In particular, the alignment of anisotropic nanoscale objects is one key prerequisite in materials science when fabricating materials and devices with anisotropic physical properties. For example the absorbance, refractive index, conductivity, and tensile strength are known to differ when measured along different directions in 3D space [231]. Techniques developed for this purpose [232] include the use of evaporation [233], space confinement [234], shear force [235], electric field [236], magnetic field [237], mechanical stretching [238], or a mixture of them [239]. For example, the hierarchical organization via convective evaporation has generated beautifully organized patterned surfaces from non-chiral inorganic anisotropic objects such as nanowires and nanorods [240].

1.4.2 Chiral Organization of Achiral Objects

The above chiral assemblies are mainly related to the chiral source such as chiral ligands or CP light. Other chiral assemblies were also reported without any chiral source. In 2014 [241], Klajn reported the helical self-assembly of magnetite Fe_3O_4 nanocubes at air/liquid interfaces (Figure 17a). These Fe_3O_4 NPs have a cubic shape with average edge length around 13 nm. Without external magnetic fields, the NPs self-assemble into belts due to the shape anisotropy (favoring face-to-face interactions). When an external magnetic field is applied, the magnetite NPs self-assemble into helical superstructures due to the competition between the shape anisotropy and magnetocrystalline anisotropy

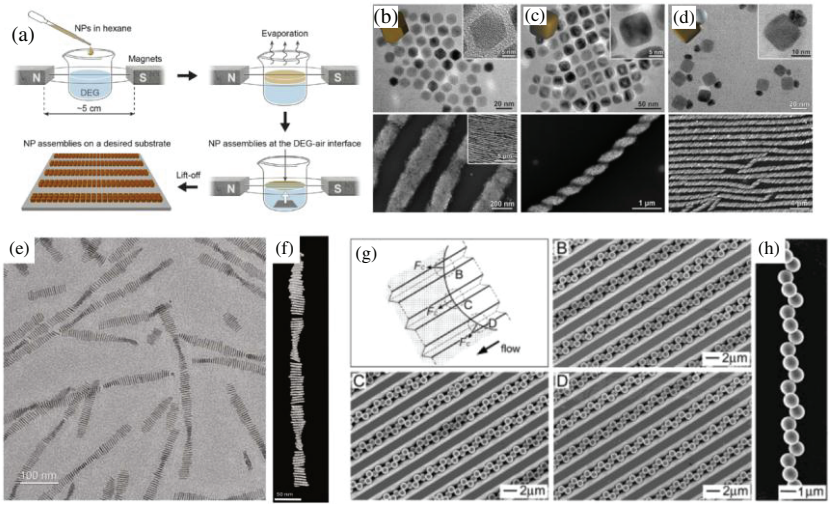

Figure 17. (a) Schematic representation of the experimental setup for self-assembly of magnetic Fe_3O_4 nanocrystals. (b) TEM images of truncated octahedrons (top) and SEM images of 1D belts as they assemble (bottom). (c) TEM images of rounded cubes (top) and an SEM image of the resulting helix (bottom). (d) TEM images of Fe_3O_4-Ag heterodimeric NCs (top) and an SEM image of an ensemble of helices (bottom). (e) TEM image of twisted ribbons of self-assembled CdSe NPLs. (f) 3D model from the tomographic reconstruction of a twisted ribbon. (g) SEM images of helical chains with different chiralities that were obtained with the capillary forces oriented toward different directions relative to the longitudinal axis of the V-grooves. (h) SEM image of a free-standing helical aggregate after it had been welded by thermal annealing and subsequently released from the original V-grooves.

(favoring corner-to-corner interactions). Figure 17b shows how the shape of Fe_3O_4 NPs affects the morphologies of the self-assembly under external magnetic fields, truncated octahedrons self-assemble into belts, while rounded cubes and Fe_3O_4-Ag heterodimeric NCs self-assemble into helical superstructures. These helical self-assemblies also have self-sorting effects and form conglomerate-type mixtures of right-handed and left-handed self-assemblies. Interestingly at high coverage, the entire domain may consist of one-handed self-assemblies, the probability of having one handedness with respect to the other handedness being equal. CdSe nanoplatelets (NPLs) can similarly self-assemble into conglomerate chiral ribbons by adding the achiral ligand oleic acid [242] (Figure 17e).

We also note an interesting report in which Xia *et al*. showed that spherical polystyrene beads with a particle size around several hundred nanometers could organize into helical structures when confined in V-shaped grooves [243] (Figure 17g). The authors reported that a helical organization of these spherical particles was observed when the ratio between the width of the V-grooves and the diameter of the colloids falls between 2.7 and 2.85. The handedness of these helical organizations could be controlled by the relative orientation of the capillary force with respect to the longitudinal axis of the helices, where the capillary force is created by the meniscus of the liquid during the filling of the particles in aqueous suspension into the grooves. The capillary force oriented to the right direction (region B) results in a left-handed helical self-assembly, while the capillary force oriented to the left direction (region D) results in a right-handed helical self-assembly. Meanwhile, when the capillary force is oriented to the middle part (region C), both right- and left-handed helical ribbons could be observed.

Inorganic nanocrystals can also be self-assembled into superstructures by various inter-particle forces, such as van der Waals forces, electrostatic forces, magnetic interactions, molecular surface forces, and entropic effects [244]. Chiral superstructures could also be obtained under certain conditions.

In 2010 [245], Kotov *et al*. showed that CdTe NPs self-assemble into flat ribbons which then transform to twisted ribbons when illuminated by visible light. This chiral self-assembly is driven by the balance between inter-nanoparticle attraction and electrostatic repulsion. However, the

self-assembled twisted ribbons are racemic with equal right-handed and left-handed twisted ribbons due to the absence of a chiral source. In order to get nonzero enantiomeric excess (ee) values, right- or left-handed CP light was applied to obtain right- or left-handed twisted ribbons [246]. The CdTe QDs stabilized with the achiral capping agent thioglycolic acid (TGA) could self-assemble into predominantly right- or left-handed twisted ribbons under right or left CP light illumination with an ee value of 0.3 (Figure 18a). Figure 18b and c shows the 3D tomographic reconstruction and SEM images of left- and right-twisted ribbons with around an 800 nm pitch.

Recently, gold NP chiral self-assembly driven by CP light illumination was reported [247]. Subsequently, the nanoparticle chiral self-assembly was optimized to get higher ee values. Interestingly, the CdTe NPs with chiral ligands have a chiral self-sorting effect. The racemic mixture of D- and L-cysteine CdTe assembled structures contained both left- and

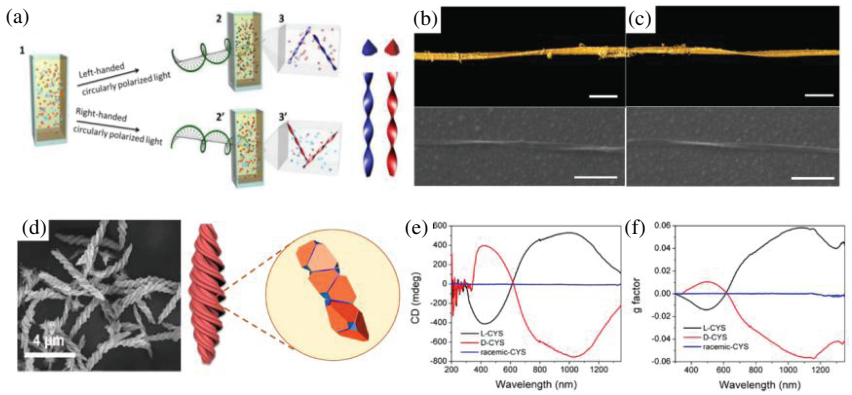

Figure 18. (a) Schematics of the CP light-induced self-assembly process. 1. Racemic mixture of CdTe QDs capped with L- and D-cysteine is prepared. 2. Left-handed CP light selectively activates left-handed NPs. 2′. Right-handed CP light activates right-handed NPs. 3. The excited left-handed NPs are self-assembled into left-handed nanoribbons. 3′. Right-handed NPs are self-assembled into right-handed nanoribbons. (b) and (c) show the surface rendering of 3D TEM tomographic reconstruction and SEM images of single left-handed and right-handed nanoribbons separately. (d) SEM image of CdTe helical superstructure by self-assembly (left) and the origin of enantiopurity in NP assembly into helices (right). (e) and (f) show the CD and g-factor of CdTe helical superstructure self-assembled by L-cys-CdTe NPs, D-cys-CdTe NPs and racemic cys-CdTe NPs.

right-handed helices with no straight ribbons observed (conglomerate-type mixture), that is, the CdTe NPs tend to self-assemble with NPs of the same chirality. The geometry of the helices can be precisely controlled by the solvent [248], pH [249], chiral ligand density, and coordination bridges between NPs [250]. The helical ribbons obtained by CdTe nanocrystal self-assembly can show dissymmetric g-factors as high as 0.06 (Figure 18f).

1.4.3 Organization/Alignment of Chiral Objects

Meanwhile, there are much fewer examples of the alignment of anisotropic chiral particles leading to the design of materials which couple the chirality of the constituent chiral elements and collective properties due to the anisotropic orientation [251].

Self-assemblies of rod-like viruses [252] or cellulose nanocrystals (CNCs) [253] have been used as model systems to design functional materials such as chiral photonic structures. Both are bio-renewable resources that spontaneously organize into chiral liquid crystals with hierarchical structures. Kuncicky *et al*. have shown that a shear-induced alignment can be obtained by pulling a meniscus containing the virus suspension over a substrate for convective nanoparticle assembly.

The periodic, chiral nematic organization of CNC films obtained by self-assembly in water show iridescence and are increasingly used for applications such as cosmetics or photonics. Such chiral organization can also be obtained via controlled evaporation under capillary confinement. Cherpak *et al*. have shown large uniformly aligned chiral photonic films could be obtained from a liquid crystal phase formed by a CNC suspension placed in a thin capillary. The confinement of CNCs during the drying process induced a coexistence of isotropic and chiral phases separated by an interface aligned perpendicular to the long axis of the capillary: the saturation of water vapor in one end of the capillary causes anisotropic drying and promotes unidirectional propagation of the anisotropic phase in large regions that results in chiral CNC solid films with uniformly oriented layered morphology (Figure 19) [254].

Recently, convective evaporation forces have been used in the dip-coating technique, to align synthetic inorganic chiral nanoobjects, namely, silica

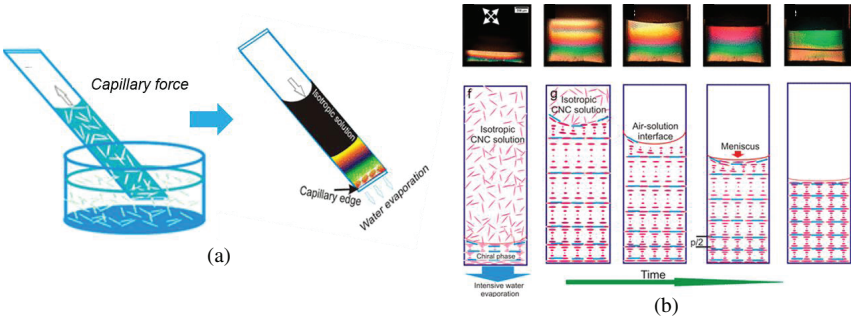

Figure 19. Special confinement process: (a) filling the rectangular capillary with a CNC suspension and immediately transferring to the optical microscope for real-time drying monitoring, and (b) real-time drying monitoring using a polarized optical microscope at 15 min, 120 min, 128 min, 131 min, and 136 min. The polarizer was placed at 45° to the capillary edge. Adapted with permission from Nano Lett. 2018, 18, 11, 6770–6777. Copyright © 2018, American Chemical Society.

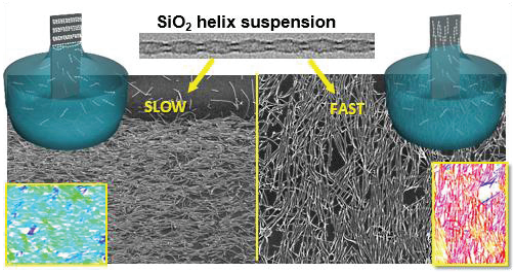

Figure 20. Controlling orientation through withdrawal speed. Left: Horizontal alignment and stick-slip layered organization with low withdrawal speed. Right: Vertical alignment for high withdrawal speed. SEM images. Silica helices orientation measured via Image J giving order parameter S = 0.95 and 0.75, respectively. Scale bars are 1 μm. Adapted with permission from [255].

nanohelices [255]. Nanoscale helices with a large aspect ratio showed an excellent coupling of shear forces in liquid with helical particle motion. The coupling of evaporation forces and physicochemical solution properties induce specific helix alignment, and the stick–slip phenomenon produces a periodical deposition of bands with controllable and regular spacing. (Figure 20).

Multilayered chiral nanostructures can be obtained by top-down lithographic fabrication techniques [256]. While these techniques are powerful in creating organized and highly controlled nanostructures such as arrays and

layered plates, they are non-scalable for sizes above 100 nm, and are time-consuming and generally costly. In contrast, bottom-up methods are often faster, less expensive, and more adaptable for arbitrary structural geometries in a larger range of scales [257]. As we have shown previously, chiral films can be made from chirally arranged particles. Among the various deposition methods of particles assemblies, layer-by-layer (LbL) deposition coupled with or without Grazing Incidence Spraying gives an interesting approach for the formation of thin films with hierarchically organized chiral NPs to "design" the spectrum of rotatory optical activity [258].

1.5 Circular Dichroism and Circular Birefringence Measurements in Solid State

The development of spectroscopic techniques (CD, CP luminescence, Raman optical activity, circular photoelectron dichroism, harmonic generation, optical vortices, optofluidic selectivity) and other techniques (X-rays based techniques, mass spectrometry, nuclear magnetic resonance, electron microscopy), is crucial to characterize these new objects, phenomena, and interactions. Among which CD and circular birefringence measurements form powerful analysis methods to quantify the chirality of the systems

1.5.1 Mueller Matrix Formalism

Circular dichroism and birefringence, which are related to the difference between the propagation of left- and right-handed circular polarizations, can be viewed as the fingerprints of chirality. Due to their small magnitudes, their measurements require advanced polarimetric instrumentation. To design an adequate polarimeter, we must evaluate the impact of each optical element on the polarization state of light. In 1948, Hans Mueller developed a matrix formalism to model the evolution of the polarization state of light during its propagation, which is now considered the precursor of modern developments in polarimetry. In addition, the Mueller matrix of a sample contains all the information concerning the sources of dichroism and birefringence. Thus, the measurement of the Mueller matrix is crucial to investigate the optical properties of chiral materials in

the solid state. Before introducing the polarimetric set up, we will give a description of the Mueller matrix formalism.

The change of the polarization state of light induced by chiral materials is investigated in the framework of the Mueller matrix formalism [259]. In this formalism, all polarization states of light can be described by the so-called Stokes vector given by:

$$S = \begin{pmatrix} I_{tot} \\ I_X - I_Y \\ I_{45^\circ} - I_{-45^\circ} \\ I_L - I_R \end{pmatrix} \tag{1}$$

Where I_{tot} is the total intensity of light. I_X, I_Y, I_{45°, I_{-45°, I_L and I_R are the intensities measured by an ideal polarizer oriented along two directions, Ox, Oy (perpendicular to the propagation of light direction Oz), the direction at 45° and –45° with respect to the Ox direction, and by left and right circular polarizers, respectively. Thus, the Stokes vector is built with measurable quantities. The Stokes vector, after being normalized by I_{tot}, can be rewritten as:

$$S = \begin{pmatrix} 1 \\ S_1 \\ S_2 \\ S_3 \end{pmatrix} \tag{2}$$

The components of the Stokes vector must respect the following sum rules:

$$1 \geq \sqrt{S_1^2 + S_2^2 + S_3^2} \tag{3}$$

The equality sign in (3) holds only if the light beam is totally polarized. In other words, each polarization state can be represented in 3-dimensional space (S_1, S_2, S_3) limited by a sphere of radius 1, called the Poincaré sphere (Figure 21a). We can define different loci in the Poincaré sphere. Pure polarization states are distributed on the surface of the Poincaré sphere while partially polarized states are located inside. All linear polarization states are located on the equator. The north and the south poles are related to the right and left polarization states, respectively.

Two orthogonal polarizations are centrosymmetrically distributed in this space.

The transmission of light through an anisotropic medium induces a change of polarization state. In other words, we can define two Stokes vectors S_{in} and S_{out}, related to the incident and transmitted polarization, respectively (Figure 21b). These Stokes vectors are linked together by a linear equation:

$$S_{out} = MS_{in} \tag{4}$$

where M is a 4×4 matrix called the Mueller matrix. Its 16 real elements (m_{ij}) connect the input and output Stokes vectors after the interaction of light with an optical medium. In other words, the Mueller matrix can be represented as a transformation operating on the Stokes vectors in the Poincaré sphere. The Mueller matrix contains all information concerning the anisotropy of the medium. Applying the condition (3) to the Mueller matrix, we can introduce a parameter P, which quantifies the degree of polarization of light:

$$P = \frac{\sqrt{Tr\left(M^T M\right) - m_{00}^2}}{\sqrt{3} m_{00}} \tag{5}$$

m_{00} is the first element of the Mueller matrix M. The value of P varies from 0 (for non-depolarizing medium) to 1 (for completely depolarizing medium). The Mueller matrix, which describes the propagation of light through a series of optical elements, is equal to the product of the Mueller matrix of each element (M_i) (Figure 21c). If we focus our attention on the incident and the emergent polarization, the overall effect of an entire cascade of N optical elements is described by:

$$S_{out} = M_N M_{N-1} \ldots M_2 M_1 S_{in} = MS_{in} \text{ with } M = \prod_{i=1}^{N} M_i \tag{6}$$

Thus, the Mueller matrix formalism is a suitable tool to describe the evolution of the polarization state of light during the propagation through an optical setup. We can now define the Mueller matrix of usual optical elements such as a linear polarizer (M_P) oriented along the Ox direction,

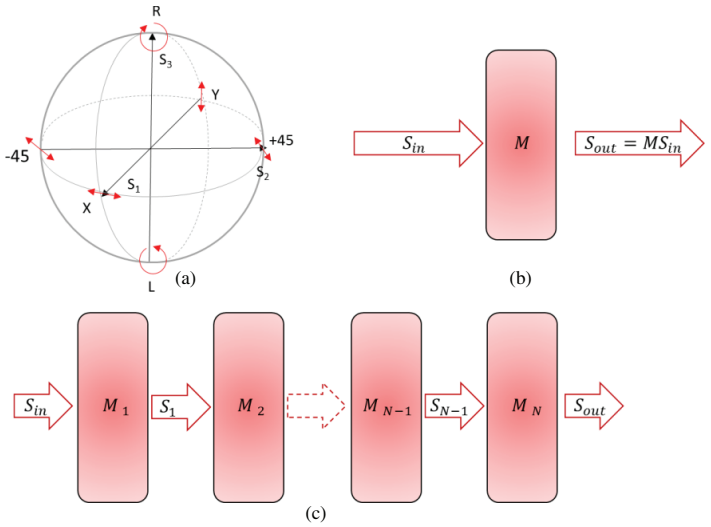

Figure 21. (a) Representation of polarization state of light in the Poincaré sphere. Change of the polarization state after the propagation though (b) a medium and (c) a stack of N media.

and a perfect retarder (M_r) whose fast axis is oriented along the Ox direction:

$$M_P = \frac{1}{2}\begin{pmatrix} 1 & 1 & 0 & 0 \\ 1 & 1 & 0 & 0 \\ 0 & 0 & 0 & 0 \\ 0 & 0 & 0 & 0 \end{pmatrix}, \quad \text{and} \quad M_r = \begin{pmatrix} 1 & 0 & 0 & 0 \\ 0 & 1 & 0 & 0 \\ 0 & 0 & \cos\delta & \sin\delta \\ 0 & 0 & -\sin\delta & \cos\delta \end{pmatrix} \tag{7}$$

Where δ is the phase difference between the fast and slow axis. The rotation of optical elements by an angle θ induces a modification of its Mueller matrix. The Mueller matrix obtained after the rotation M_{rot} is expressed as:

$$M_{rot} = R(-\theta)MR(\theta) \tag{8}$$

with $R(\theta) = \begin{pmatrix} 1 & 0 & 0 & 0 \\ 0 & \cos(2\theta) & \sin(2\theta) & 0 \\ 0 & -\sin(2\theta) & \cos(2\theta) & 0 \\ 0 & 0 & 0 & 1 \end{pmatrix}$ the rotation matrix.

Thus, the Mueller matrix formalism is a powerful tool to describe the change of polarization state of light induced by an optical setup.

1.5.2 Differential Decomposition

Mueller matrices can be phenomenologically interpreted by decomposing them into simple polarimetric parameters. Several decompositions have been proposed in the literature [260]. Differential decomposition is a powerful tool when the light is transmitted by a homogeneous medium. By considering the linear differential propagation equation, the Mueller matrix M of a medium with an optical thickness l is related to a differential matrix:

$$\frac{dM(l)}{dl} = mM(l) \tag{9}$$

By solving equation 9, we find:

$$M(z) = \exp(ml) = \exp(L) \tag{10}$$

L is a 4×4 matrix, which can be decomposed into a sum of a depolarizing matrix (L_u) and a non-depolarizing matrix (L_m) [260a]:

$$L = L_m + L_u, \qquad \text{with} \begin{cases} L_m = \frac{1}{2}\left(L - GL^T G\right) \\ L_u = \frac{1}{2}\left(L + GL^T G\right) \end{cases} \tag{11}$$

where G = diag(1,–1,–1,–1) is the Minkowski metric. The matrix L_m can be expressed as:

$$L_m = \begin{pmatrix} 0 & -LD & -LD' & CD \\ -LD & 0 & CB & LB' \\ -LD' & -CB & 0 & -LB \\ CD & -LB' & LB & 0 \end{pmatrix} \tag{12}$$

Where LD and LD′ are linear dichroisms along Ox-Oy and ±45° axes, LB and LB′ are linear birefringences along Ox-Oy and ±45° axes respectively, CD is circular dichroism and CB is circular birefringence. These polarimetric parameters are related to the complex refractive indices of the medium:

$$LB = 2\pi\bar{\nu}l\left(n_x - n_y\right) \tag{13}$$

$$LD = 2\pi\bar{\nu}l\left(k_x - k_y\right) = \frac{\ln(10)}{2}\left(A_x - A_y\right) \tag{14}$$

$$LB' = 2\pi\bar{\nu}l\left(n_{45} - n_{-45}\right) \tag{15}$$

$$LD' = 2\pi\bar{\nu}l\left(k_{45} - k_{-45}\right) = \frac{\ln(10)}{2}\left(A_{45} - A_{-45}\right) \tag{16}$$

$$CB = 2\pi\bar{\nu}l\left(n_L - n_R\right) \tag{17}$$

$$CD = 2\pi\bar{\nu}l\left(k_L - k_R\right) = \frac{\ln(10)}{2}\left(A_L - A_R\right) \tag{18}$$

Where $\bar{\nu}$ is the wavenumber, n_i is the real part of the refractive index, k_i is the imaginary part of the refractive index and A_i ($i = x$, y, 45, –45, L or R) is the absorbance of the medium for light linearly polarized along the Ox, Oy, +45° and –45° axes, and for left- and right-handed circular polarizations, respectively. For non-depolarizing chiral materials, which have a rotation symmetry, the linear dichroism and birefringence are equal to 0. According to equations 10 and 12, the Mueller matrix of this material through a first order approximation is given by:

$$M = \begin{pmatrix} m_{00} & 0 & 0 & m_{03} \\ 0 & m_{11} & m_{12} & 0 \\ 0 & -m_{12} & m_{11} & 0 \\ m_{03} & 0 & 0 & m_{00} \end{pmatrix} = \begin{pmatrix} 1 & 0 & 0 & CD \\ 0 & 1 & CB & 0 \\ 0 & -CB & 1 & 0 \\ CD & 0 & 0 & 1 \end{pmatrix} \tag{19}$$

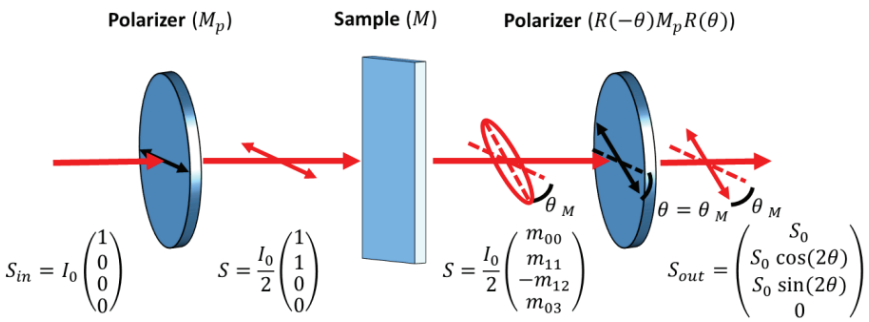

Figure 22. Measurement of optical rotation induced by an active medium.

1.5.3 Determination of CB from the Optical Rotation

According to the definition of CB (equation 17), right and left circular polarizations propagate inside an optically active medium at different speeds. In other words, the phase relationships between the two circularly polarizing waves changes. As linear polarization is a superposition of a right and left circular polarization, the CB induces a rotation of the linearly polarized wave. Before the advent of modern CD polarimeters, the optical activity of chiral molecules was commonly determined by measuring this optical rotation (OR). As illustrated in Figure 22, the simplest OR set up is composed of two linear polarizers, with the sample placed between them. The Stokes vector (S_{out}) of the transmitted light through the optical set up is given by:

$$S_{out} = \begin{pmatrix} S_0 \\ S_1 \\ S_2 \\ S_3 \end{pmatrix} = R(-\theta) M_p R(\theta) M M_p \begin{pmatrix} 1 \\ 0 \\ 0 \\ 0 \end{pmatrix} I_0 \tag{20}$$

By assuming that the chiral material does not exhibit depolarization as well as linear dichroism and birefringence, its Mueller matrix (M) is given by equation 19. The intensity of light measured by the detector at a wavenumber $\bar{\nu}$ is given by the first element of the transmitted Stokes vector (S_0):

$$S_0(\bar{\nu}) = \frac{I_0}{4}(1 + \cos(2\theta) - CB(\bar{\nu})\sin(2\theta)) \tag{21}$$

The second polarizer is rotated to find the angle θ_M, which maximizes the intensity of light measured by the optical sensor. Then, the CB at a given wavenumber $\bar{\nu}$ is directly given by: $CB(\bar{\nu}) = -2\theta_M$

Large amounts of chiral materials are optically active, that is, they exhibit CD and CB. $CB(\bar{\nu})$ *and* $CD(\bar{\nu})$ are linked together by the Kramers–Kronig relations:

$$CD(\bar{\nu}_a) = -\frac{2\bar{\nu}_a}{\pi} P \int_0^{\infty} \frac{CB(\bar{\nu})}{\bar{\nu}^2 - \bar{\nu}_a^2} d\bar{\nu} \tag{22}$$

$$CB(\bar{\nu}_a) = \frac{2}{\pi} P \int_0^{\infty} \frac{\bar{\nu} \cdot CD(\bar{\nu})}{\bar{\nu}^2 - \bar{\nu}_a^2} d\bar{\nu}. \tag{23}$$

We can conclude that $CB(\bar{\nu})$ and $CD(\bar{\nu})$ bring the same information. However, the use of the Kramers–Kronig relation requires knowledge of the CD or the CB at all wavenumbers. As the spectral range of CB measurements is always limited, $CD(\bar{\nu})$ cannot be easily estimated from $CB(\bar{\nu})$. Therefore, it is suitable to use an experimental set up which measures simultaneously the $CD(\bar{\nu})$ and $CB(\bar{\nu})$ spectra.

1.5.4 Determination of Circular Dichroism (CD) and Circular Birefringence (CB) by a UV-visible or Infrared Spectrometer

The CD of an isotropic non-depolarizing medium is related to the difference between the absorption coefficient of left and right circular polarizations. However, the CD of natural materials, which is in the order of 10^{-5}–10^{-4}, is too small to be directly measured from polarized absorption spectroscopy. Most modern instruments are based on a polarization–modulation approach. As shown in Figure 23a, the light emitted by the source passes through a cascade of optical compounds: a polarizer oriented at 45°, a photoelastic modulator (PEM) and the sample. Typical PEMs consist of a piezoelectric transducer mounted to the sides of a fused silica (UV-Visible) or a ZnSe (infrared) crystal. A voltage applied to the transducer creates strains, and so a linear birefringence in the silica (or ZnSe) crystal. The PEM is a perfect retarder whose Mueller matrix M_r is defined by equation 7. The phase difference δ between the fast and slow axis depends on the applied voltage. Thus, the following variable retardation can be created by application of an adequate voltage:

$$\delta(t) = \delta_M(\bar{\nu}) \sin(2\pi ft) \tag{24}$$

where $\delta_M(\bar{\nu})$ is the maximum value of the sine-wave retardation angle at the wavenumber $\bar{\nu}$. This value is adjusted for a given wavenumber $\bar{\nu}$ so as to act as a quarter-wave plate. For other wavenumbers, an efficiency function should be considered ($J_1(\delta_M(\bar{\nu}))$ described below). Generally, the

PEM operates at a frequency of 50 kHz. The Stokes vector (S_{out}) of the transmitted light through the optical set up is given by:

$$\begin{pmatrix} S_0 \\ S_1 \\ S_2 \\ S_3 \end{pmatrix} = MM_r R(-45°) M_p R(45°) \begin{pmatrix} 1 \\ 0 \\ 0 \\ 0 \end{pmatrix} I_0 \tag{25}$$

The detected intensity is given by S_0:

$$S_0(\bar{\nu}, t) = \frac{1}{2} I_0 \left(m_{00} + m_{02} \cos\delta\,(t) - m_{03} \sin\delta\,(t) \right) \tag{26}$$

According to equation 19, the detected intensity for a non-depolarizing isotropic chiral material is given by:

$$S_0(\bar{\nu}, t) = \frac{1}{2} I_0 (1 - CD(\bar{\nu}) \sin\delta\,(t)) \tag{27}$$

The CD appears in equation 27 as the amplitude of the periodic function $sin\delta(t) = \sin(\delta_M(\bar{\nu})\sin(2\pi ft))$. The full sine-wave dependence of the detected intensity is given by:

$$\sin\left(\delta\,(t)\right) = \sin\left(\delta_M(\bar{\nu})\sin\left(2\pi ft\right)\right) = \sum_{n=odd} 2J_n\left(\delta_M(\bar{\nu})\right)\sin\left(2\pi nft\right) \tag{28}$$

where the second equality is a sum over odd-order Bessel functions, J_n, at the odd harmonics of the PEM frequency nf, where n in the summation is equal to only integers starting at 1. The first term in the odd harmonic expansion above is the main CD signal at the detector. This signal, at the fundamental PEM frequency f, is measured by a lock-in amplifier tuned to f as the amplitude of $sin(2\pi ft)$, and is equal to $2J_1(\delta_M(\bar{\nu}) \cdot CD(\bar{\nu})$. The measurement of CD with a lock-in amplifier considerably improves the signal-to-noise ratio. This strategy makes CD spectroscopy a routine tool for the determination of the chirality of materials. However, a calibration procedure is necessary to determine the $J \cdot (\delta_M(\bar{\nu}))$ function in Fourier transform infrared spectroscopy [261].

To measure simultaneously the CB and the CD, a second polarizer, oriented along the Ox direction, can be added after the sample [262]. The

corresponding experimental set up is depicted in Figure 23b. The transmitted Stokes vector is given by:

$$S_{out} = \begin{pmatrix} S_0 \\ S_1 \\ S_2 \\ S_3 \end{pmatrix} = M_p M M_r R(-45°) M_p R(45°) \begin{pmatrix} 1 \\ 0 \\ 0 \\ 0 \end{pmatrix} I_0, \tag{29}$$

The variation of the detected light intensity is given by S_0:

$$S_0(\bar{\nu}, t) = \frac{I_0}{4}\left(m_{00} + m_{10} + (m_{02} + m_{12})\cos\delta\ (t) - (m_{03} + m_{13})\sin\delta\ (t)\right) \tag{30}$$

This equation can be considerably simplified for a non-depolarizing isotropic chiral material:

$$S_0(\bar{\nu}, t) = \frac{I_0}{4}\left(1 + CB(\bar{\nu})\cos\delta\ (t) - CD(\bar{\nu})\sin\delta\ (t)\right) \tag{31}$$

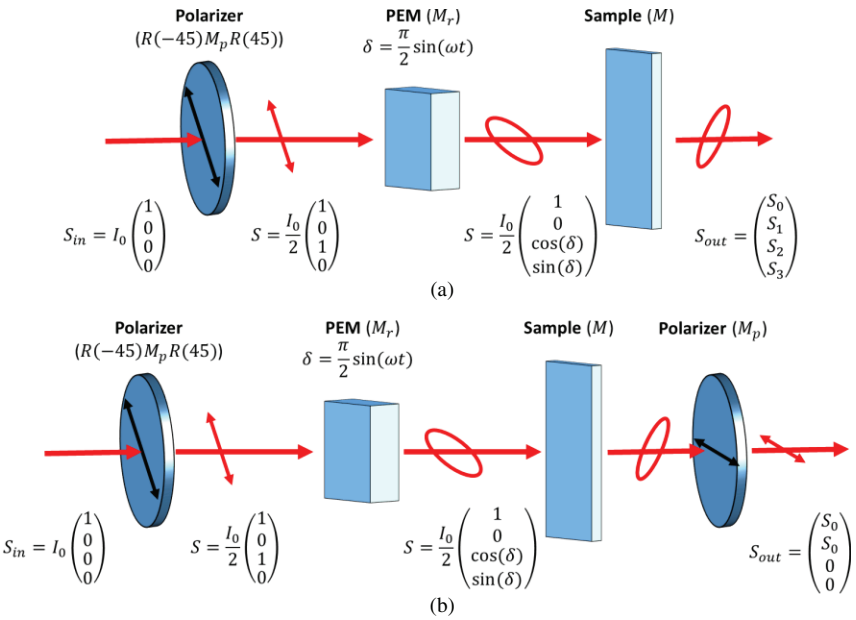

Figure 23. Experimental set up used to measure (a) the CD and (b) the CB.

On the other hand, the CB is related to the amplitude of a periodic function $\cos\delta(t) = \cos(\delta_M(\bar{\nu})\ \sin(2\pi ft))$, which has a frequency *2f*. Thus, $CD(\bar{\nu})$ and $CB(\bar{\nu})$ spectra can be determined by filtering the signal at the frequency *f* and 2*f*, respectively.

Since $\cos(\delta(t)) = \cos(\delta_M(\bar{\nu})\ \sin(2\pi ft)) = J_0(\delta_M(\bar{\nu})) + \Sigma_{n=even} 2J_n(\delta_M(\bar{\nu}))\ \cos(2\pi nft)$, the CB signal measured by a lock-in amplifier tuned to 2f is equal to $2J_2(\delta_M(\bar{\nu}) \cdot \mathrm{CB}(\bar{\nu})$

Despite their high sensitivity, these instruments have several limitations [263]. It can only be used to determine the $CD(\bar{\nu})$ and $CB(\bar{\nu})$ and spectra of a non-depolarizing isotropic sample. However, a large number of natural and artificial chiral materials present anisotropy, particularly in the solid state. These materials thus simultaneously exhibit an optical activity and a linear anisotropy (i.e., linear birefringence (LB) and linear dichroism (LD)). In this case, the Mueller matrix cannot be simply written as equation 19 and the m_{03} and m_{12} elements, determined from the instruments shown in Figure 3, are a complex combination of LB, LB′, LD, LD′, CD, and CB. In other words, the presence of linear dichroism and linear birefringence create artifacts in the measured CD and CB.

1.5.5 Determination of Circular Dichroism (CD) for Samples Exhibiting Linear Birefringence and Linear Dichroism

To determine the measured CD of a chiral material exhibiting LB and LD in the plane of the sample, it is necessary to take into account several imperfections of the optical set up described in Figure 22a, such as the residual static birefringence of the PEM, δ_0, and the different responses of the detector along the *x* and *y* axes. The residual static birefringence of the PEM modifies the Mueller matrix M_r as:

$$M_r = \begin{pmatrix} 1 & 0 & 0 & 0 \\ 0 & 1 & 0 & 0 \\ 0 & 0 & cos(\delta + \delta_0) & sin(\delta + \delta_0) \\ 0 & 0 & -sin(\delta + \delta_0) & cos(\delta + \delta_0) \end{pmatrix}, \tag{32}$$

An additional Mueller matrix is used for the non-perfect detector, $D(\alpha)$, which is given by :

$$D(\alpha) = \begin{pmatrix} (p_x^2 + p_y^2) & (p_x^2 - p_y^2)cos2\alpha & (p_x^2 - p_y^2)sin2\alpha & 0 \end{pmatrix} \quad (33)$$

where p_x and p_y are the different responses of the detector to radiation polarized along its local x and y axes, respectively, and where these local axes are oriented at an angle α with respect to the Ox axis.

Considering that the maximum linear dichroism is along the Ox direction, referred by the angle $\theta = 0°$ (the θ angle stands for the rotation of the sample around the Oz axis corresponding to the direction of the radiation), the 45° linear birefringence (LB′) and linear dichroism (LD′) are equal to zero in the general Mueller matrix of the sample. Moreover, assuming that (CD, CB) << (LD, LB) << 1 and that sin δ_0 and $(p_x^2 - p_y^2)$ << 1.0, the CD signal measured by a lock-in amplifier tuned to f is equal to [264]:

$$2J_1(\delta_M(\bar{\nu}))\left[(CD(\bar{\nu})\cos\delta_0 - LD(\bar{\nu})\cos2\theta\sin\delta_0) + \left(\frac{p_x^2 - p_y^2}{p_x^2 + p_y^2}\right)LB(\bar{\nu})\cos\delta_0(\sin2\theta\cos2\alpha - \cos2\theta\sin2\alpha)\right] \quad (34)$$

Equation 34 shows that the measured $CD(\bar{\nu})$ spectrum contains not only the CD of the sample but also linear dichroism and birefringence contributions. The LD contribution is connected to the residual static birefringence introduced by the PEM, whereas the LB contribution is related to polarization imperfections of the detector. This means that it is important to measure LD as well as LB when looking for the true CD spectrum of a sample possessing macroscopic anisotropy. Also, even for achiral samples (i.e., CD=0) a false $CD(\bar{\nu})$ spectrum can be measured when the sample possesses large LD and LB contributions. Generally, the value of $sin\delta_0$ is around 0.001, and consequently the $cos\delta_0$ term is close to 1.

A detailed examination of equation 34 shows that the LD and LB contributions are involved in "$cos2\theta$" and "$sin2\theta$"periodic functions of the sample rotation. Thus, the half-sum of two experimental $CD(\bar{\nu})$ spectra for

sample orientations at θ and $\theta \pm 90°$ represents a rapid and simple way to extract the true CD contribution:

$$CD_{true} = \frac{CD(\theta) + CD(\theta \pm 90°)}{2} \tag{35}$$

1.5.6 Mueller matrix Polarimetry

The complete Mueller matrix is required to investigate the optical activity of complex chiral materials. Its determination is achieved by a Mueller matrix polarimeter illustrated in Figure 24. The sample is sandwiched between a polarization state generator (PSG) and a polarizer state analyzer (PSA). Several configurations of PSGs and PSAs are proposed in the literature. The most common are listed in Table 1. The PSG generates a set of input Stokes vectors S_{PSG}, which are transformed by the sample into $S_s = MS_{PSG}$. This Stokes vector is then analyzed by the PSA, which delivers a Stokes vector S_{out} given by:

$$S_{out} = \begin{pmatrix} S_0 \\ S_1 \\ S_2 \\ S_3 \end{pmatrix} = M_{PSA} M M_{PSG} \begin{pmatrix} 1 \\ 0 \\ 0 \\ 0 \end{pmatrix} I_0 \tag{36}$$

where M, M_{PSG}, and M_{PSA} are the Mueller matrices of the sample, the PSG and the PSA. The first element of S_{out} is the intensity of light measured by the detector:

$$S_0 = \begin{pmatrix} m_{00,PSA} & m_{01,PSA} & m_{02,PSA} & m_{03,PSA} \end{pmatrix} \begin{pmatrix} m_{00} & m_{01} & m_{02} & m_{03} \\ m_{10} & m_{11} & m_{12} & m_{13} \\ m_{20} & m_{21} & m_{22} & m_{22} \\ m_{30} & m_{31} & m_{32} & m_{33} \end{pmatrix} \begin{pmatrix} m_{00,PSG} \\ m_{10,PSG} \\ m_{20,PSG} \\ m_{30,PSG} \end{pmatrix}. \tag{37}$$

Figure 24. Schematic representation of a Mueller matrix polarimeter.

Table 1. Common structures of PSAs and PSGs.

Configuration	Characteristics	Drawback
A polarizer + a rotating quarter-wave plate (QWP) [265]	• Fixed retardation rotation to change the azimuth of the QWP	• QWP are not completely achromatic • Small modulation frequency due to the mechanical rotation
A polarizer + two liquid crystal cells (LCs) [266]	• Variable retardation for nematic LC • Variable azimuth for ferroelectric LC	• Cannot be used in UV • Temperature dependence • No frequency domain analysis
A polarizer + a rotating PEM [267]	• Fast modulation • Variable retardation • Broad spectral range	• Mechanical rotation • Temperature dependence
A polarizer+ two PEMs [268]	• Fast modulation • Variable retardation • Fixed azimuth • Broad spectral range • No mechanical rotation	• Temperature dependence

m_{ij}, $m_{ij,PSG}$ and $m_{ij,PSA}$, with $i,j = 0,1,2,3$, are the elements of the Mueller matrix of the sample, the PSG and the PSA. Basically, there are two approaches to measure the Mueller matrix of the sample. The first one consists in changing the parameters $m_{ij,PSG}$ and $m_{ij,PSA}$ of the PSG and the PSA at different frequencies. A Fourier transform is performed on the variation of measured intensity. The Mueller matrix elements are then deduced from the amplitudes of all relevant frequency harmonics. In the second approach, several intensity measurements are performed for different configurations of PSG and PSA. According to equation 37, a combination of 4 PSA configurations and 4 PSG configurations are required to obtain all the Mueller matrix elements of the sample.

The differential decomposition of the complete Mueller matrix offers the unique capacity to separate polarizing and depolarizing effects. This method allows the evaluation of all polarimetric parameters such as CD, CB, LB, or LD. Thus, Mueller matrix polarimetry is nowadays an essential tool for investigating the change of polarization of light induced by biological [269] or artificial materials [258b, 270].

References

1. Bonner, W.A. (1991) *Origins of Life and Evolution of the Biosphere*, **21**, 59.
2. Ariëns, E.J. (1984) *Eur. J. Clin. Pharmacol.*, **26**, 663
3. Calcaterra, A.*, et al*. (2018) *J. Pharm. Biomed. Anal.*, **147**, 323.
4. Francotte, E., *et al*. (2006) *Chirality in Drug Research,* Vol. 33, Wiley-VCH Verlag GmbH & Co.
5. Lin, G.Q., *et al*. (2011) *Chiral Drugs: Chemistry and Biological Action*, John Wiley & Sons, Inc.
6. Lorenz, H., *et al*. (2014) *Angew. Chem. Int. Ed.*, **53**, 1218.
7. Wang, Y., *et al*. (2008) *Org. Process. Res. Dev.*, **12**, 282.
8. Suwannasang, K., *et al*. (2017) *Org. Process. Res. Dev.*, **21**, 623.
9. Bredikhin, A.A., *et al*. (2017) *Chem. Eng. Technol.*, **40**, 1211.
10. J. M. McBride, *et al*. (1991) *Angew. Chem. Int. Ed.*, **30**, 293.
11. Mauskopf, S.H. (1976) *Trans. Am. Philos. Soc.*, **66**, 1.
12. Biot, J.-B. (1817) *Mém. Acad. Sci.*, **2**, 41.
13. Mason, S.F. (1982) *Molecular Optical Activity and the Chiral Discriminations*, Cambridge University Press.
14. Biot, J.-B. (1844) *C. R. Acad. Sci. Paris*, **19**, 719.
15. Pasteur, L. (1848) *Ann. Chim. Phys.*, **24**, 442.
16. Pasteur, L., (1849) *Ann. Chim. Phys. 3e série, tome XXVIII, 56*
17. Pasteur, L. (1852) *Ann. Chim. Phys.,* **34**, 30.
18. Piutti, A. (1886) *Ber. Dtsch. Chem. Ges.*, **19**, 1691.
19. Piutti, A. (1888) *Gazz. Chim. Ital.*, **18**, 457.
20. Gal, J. (2012) *Chirality*, **24**, 959.
21. Rooseboom, H.W.B. (1899) *Z. Physik. Chem.*, **28**, 494.
22. Wallach, O. (1895) *Liebigs Ann. Chem.*, **286**, 90.
23. a) Blazis, V.J., *et al*. (1997) *Acta Crystallogr. B*, **53**, 838; b) Brock, C.P., *et al*. (1991) *J. Am. Chem. Soc.*, **113**, 9811; c) Friščić, T., *et al*. (2008) *Chem. Commun.*, 1644; d) Kitaigorodskii, A.I. (1965) *Acta Crystallogr.*, **18**, 585; e) Wu, X., *et al*., (2020) *Nat. Commun.*, **11**, 2145.
24. a) Dunitz, J.D., *et al*. (2012) *J. Phys. Chem. B*, **116**, 6740; b) Gavezzotti, A., *et al*. (2014) *J. Org. Chem.*, **79**, 8; c) Jeong, K.S., *et al*. (2009) *Tetrahedron Asymmetry*, **20**, 1736; d) Kennedy, A.R., *et al*. (2011) *Cryst. Growth Des.*, **11**, 1821; e) Patrick, B.O., *et al*. (2006) *Acta Crystallogr. B*, **62**, 488.
25. Jacques, J., *et al*., (1981) *Enantiomers, Racemates, and Resolutions*, J. Wiley & Sons, Inc.
26. A. Otero-de-la-Roza, *et al*., (2016). *Cryst. Growth Des.,* 5.
27. a) Diniz, L.F., *et al*. (2019) *Cryst. Growth Des.*, **19**, 4498; b) Huang, J., *et al*. (2006) *J. Am. Chem. Soc.*, **128**, 11985; c) Rekis, T., *et al*. (2018) *Cryst. Growth Des.*, **18**, 264.
28. a) Coquerel, G. (2000) *Enantiomer*, **5**, 481; b) Coquerel, G. (2007) *Novel Optical Resolution Technologies,* K. Sakai, N. Hirayama, and R. Tamura (Eds.), Springer,

pp. 1; c) Coquerel, G., *et al*. (2020) *Symmetry,* **12**, 1796; d) Secor, R.M. (1963) *Chem. Rev*. 63, 297.
29. a) Jacques, J., *et al*. (1981) *Tetrahedron*, **37**, 1727; b) Landrieu, P. (1922) *Bull. Soc. Chim. France*, **31**, 1217; c) Li, Z.J., *et al*. (1999) *J. Pharm. Sci.*, **88**, 337.
30. Saha, M.K., *et al*. (2002) *Cryst. Growth Des.*, **2**, 205.
31. Flack, H.D. (2003) *Helvetica Chimica Acta*, **86**, 905.
32. Clevers, S., *et al*. (2013) *J. Therm. Anal. Calorimet.*, **112**, 271.
33. Newman, A.C.D., *et al*. (1952) *J. Chem. Soc.*, **3747**.
34. Devogelaer, J.-J., *et al*. (2020) *Angewandte Chemie*, **132**, 21895.
35. Srisanga, S., *et al*. (2010) *Cryst. Growth Des.*, **10**, 1808.
36. Wright, A.F., *et al*. (1981) *J. Solid State Chem.*, **36**, 371.
37. Miyata, M., *et al*. (2015) *Symmetry*, **7**, 1914.
38. Bartus, J., *et al*. (1992) *Polym. Bull.*, **28**, 203.
39. Kipping, F.S., *et al*. (1898) *J. Chem. Soc. Trans.*, **73**, 606.
40. Gernez, D. (1866) *Compt. Rend. Acad. Sci.*, **63**, 843.
41. a) Collet, A., *et al*. (1980) *Chem. Rev.*, **80**, 215; b) Polenske, D., *et al*. (2009) *Chirality*, **21**, 728.
42. Fogassy, E., *et al*. (2006) *Org. Biomol. Chem.*, **4**, 3011.
43. Bolchi, C., *et al*. (2007) *Tetrahedron Asymmetry*, **18**, 1038.
44. a) Binev, D., *et al*. (2016) *Cryst. Growth Des.*, **16**, 1409; b) Dunn, A.S., *et al*. (2020) *Cryst. Growth Des.*, **20**, 7726; c) Eicke, M.J., *et al*. (2013) *Cryst. Growth Des.*, **13**, 1638; d) Galan, K., *et al*. (2015) *Cryst. Growth Des.*, **15**, 1808; e) Levilain, G., *et al*. (2012) *Cryst. Growth Des.*, **12**, 5396.
45. a) Levilain, G., *et al*. (2010) *CrystEngComm*, **12**, 1983; b) Viedma, C., *et al*. (2015) *Handbook of Crystal Growth* (Second Edition) T. Nishinaga (Ed.), Elsevier, pp. 951.
46. a) Jamison, M.M., *et al*. (1942) *J. Chem. Soc.*, 437; b) Oketani, R., *et al*. (2019) *Chem. A Eur. J.*, **25**, 13837.
47. Oketani, R., *et al*. (2019) *Org. Process. Res. Dev.*, **23**, 1197.
48. a) Belletti, G., *et al*. (2020) *Chem. A Eur. J.*, **26**, 839; b) Turner, N.J. (2010) *Curr. Opin. Chem. Biol.*, **14**, 115.
49. Rachwalski, M., *et al*. (2013) *Chem. Soc. Rev.*, **42**, 9268.
50. a) Cheng, F., *et al*. (2020) *Green Chemistry*, **22**, 6815; b) A. Hölzl-Hobmeier, *et al*. (2018) *Nature*, **564**, 240.
51. Yang, B., *et al*. (2020) *Tetrahedron Lett.*, **61**, 152530.
52. Havinga, E. (1954) *Biochim. Biophys. Acta*, **13**, 171.
53. Buhse, T., *et al*. (2021) *Chem. Rev.,* **121**, 2147.
54. Sögütoglu, L.-C., *et al*. (2015) *Chem. Soc. Rev.*, **44**, 6723.
55. Intaraboonrod, K., *et al*. (2020) *Mendeleev Commun.*, **30**, 395.
56. Xiouras, C., *et al*. (2018) *Ultrason. Sonochem.*, **43**, 184.
57. Iggland, M., *et al*. (2014) *Chem. Eng. Sci.*, **111**, 106.

58. Cameli, F., *et al*. (2018) *CrystEngComm*, **20**, 2897.
59. Kondepudi, D.K., *et al*. (1990) *Science*, **250**, 975.
60. a) Kondepudi, D.K., *et al*. (1993) *J. Am. Chem. Soc.*, **115**, 10211; b) Kondepudi, D.K., *et al*. (1992) *Phys. A Statist. Mech. Appl.*, **188**, 113; c) Kondepudi, D.K., *et al*. (1994) *Chem. Phys. Lett.*, **217**, 364.
61. Viedma, C. (2004) *J. Cryst. Grow.*, **261**, 118.
62. a) Engwerda, A.H.J., *et al*. (2018) *Angew. Chem. Int. Ed.*, **57**, 15441; b) Engwerda, A.H.J., *et al*. (2017) *Cryst. Growth Des.*, **17**, 5583; c) Noorduin, W.L., *et al*. (2009) *Angew. Chem. Int. Ed.*, **48**, 4581; d) Noorduin, W.L., *et al*. (2008) *Angew. Chem. Int. Ed.*, **47**, 6445; e) Shimizu, W., *et al*. (2020) *Cryst. Growth Des.*, **20**, 5676.
63. a) Azeroual, S., *et al*. (2012) *Chem. Commun.*, **48**, 2292; b) Björemark, P.M., *et al*. (2015) *Chem. A Eur. J.*, **21**, 10630; c) McLaughlin, D.T., *et al*. (2014) *Cryst. Growth Des.*, **14**, 1067.
64. a) Cartwright, J.H.E., *et al*. (2007) *Phys. Rev. Lett.*, **98**, 165501; b) Noorduin, W.L., *et al*. (2010) *Angew. Chem. Int. Ed.*, **49**, 8435; c) Saito, Y., *et al*. (2008) *J. Phys. Soc. Japan*, **77**, 113001; d) Suwannasang, K., *et al*. (2013) *Cryst. Growth Des.*, **13**, 3498; e) Uwaha, M. (2004) *J. Phys. Soc. Jpn*, **73**, 2601; f) Uwaha, M. (2008) *J. Phys. Soc. Jpn*, **77**, 083802.
65. a) Breveglieri, F., *et al*. (2020) *Org. Process. Res. Dev.*, **24**, 1515; b) Breveglieri, F., *et al*. (2018) *Cryst. Growth Des.*, **18**, 1873; c) Cameli, F., *et al*. (2020) *Chem. Eur. J.*, **26**, 1344; d) Li, W.W., *et al*. (2016) *Cryst. Growth Des.*, **16**, 5563; e) Maggioni, G.M., *et al*. (2018) *CrystEngComm*, **20**, 3828; f) Oketani, R., *et al*. (2018) *Cryst. Growth Des.*, **18**, 6417; g) Steendam, R.E., *et al*. (2018) *Cryst. Growth Des.*, **18**, 3008; h) Viedma, C., *et al*. (2011) *Chem. Commun.*, **47**, 12786.
66. a) Bodak, B., *et al*. (2018) *Cryst. Growth Des.*, **18**, 7122; b) Katsuno, H., *et al*. (2016) *Phys. Rev. E*, **93**, 013002; c) Suwannasang, K., *et al*. (2014) *Chem. Eng. Technol.*, **37**, 1329; d) Uchin, R., *et al*. (2017) *Chem. Eng. Technol.*, **40**, 1252.
67. Valenti, G., *et al*. (2020) *Angew. Chem. Int. Ed.* 2021, 60, 5279. https://onlinelibrary.wiley.com/doi/abs/10.1002/anie.202013502
68. Suwannasang, K., *et al*. (2016) *Cryst. Growth Des.*, **16**, 6461.
69. a) Kongsamai, P., *et al*. (2018) *Chem. Eng. Technol.*, **41**, 1173; b) Kongsamai, P., *et al*. (2017) *Eur. Phys. J. Spec. Top.*, **226**, 823.
70. Cruz, J.-M., *et al*. (2020) *Chirality*, **32**, 120.
71. a) Addadi, L., *et al*. (1985) *Angew. Chem. Int. Ed.*, **24**, 466; b) Weissbuch, I., *et al*. (1991) *Science*, **253**, 637; c) Weissbuch, I., *et al*. (1987) *J. Am. Chem. Soc.*, **109**, 1869.
72. a) Kozma, D. (2002) *CRC Handbook of Optical Resolutions Via Diastereomeric Salt Formation*. CRC Press; b) Marchand, P., *et al*. (2004) *Tetrahedron Asymmetry*, **15**, 2455.
73. Pasteur, L. (1853) *C. R. Acad. Sci.*, **37**, 162
74. Fischer, E. (1899) *Berichte der deutschen chemischen Gesellschaft*, **32**, 2451.

75. a) Bolchi, C., *et al*. (2003) *Tetrahedron Asymmetry*, **14**, 3779; b) Bolchi, C., *et al*. (2005) *Tetrahedron Asymmetry*, **16**, 1639; c) Borghese, A., *et al*. (2004) *Org. Process. Res. Dev.*, **8**, 532.
76. a) Kinbara, K. (2005) *Synlett*, 732.
77. Faigl, F., *et al*. (2008) *Tetrahedron Asymmetry*, **19**, 519.
78. San, O., *et al*. (2016) *Cryst. Growth Des.*, 16, 307.
79. King, V.L., PhD Thesis thesis, University of Zurich, 1912.
80. Lacour, J., *et al*. (2003) *Chem. Soc. Rev.*, **32**, 373.
81. a) Jeremić, D.A., *et al*. (2010) *Cryst. Growth Des.*, **10**, 559; b) Norden, B. (1972) *Acta Chem. Scand.*, **26**, 126.
82. a) Bark, T., *et al*. (2004) *Chem. A Eur. J.*, **10**, 4839; b) Garbett, K., *et al*. (1966) *J. Chem. Soc. A: Inorgan. Phys., Theor.*, **802**.
83. Ishihara, K., *et al*. (1998) *J. Am. Chem. Soc.*, **120**, 6920.
84. Wong, L.W.Y., *et al*. (2015) *Chem. Commun.*, **51**, 15760.
85. Jacques, J., *et al*. (1989) *Organic Synth.*, **67**, 1.
86. Hoffmann, S., *et al*. (2005) *Angew. Chem. Int. Ed.*, **44**, 7424.
87. Rapenne, G., *et al*. (1996) *J. Am. Chem. Soc.*, **118**, 10932.
88. a) Koenig, M., *et al*. (1979) *J. Chem. Soc. Perkin Trans.,* **2**, 40; b) Lacour, J., *et al*. (1998) *Tetrahedron Lett.*, **39**, 4825; c) Rosenheim, A., *et al*. (1925) *Berichte der deutschen chemischen Gesellschaft (A and B Series)*, **58**, 2000.
89. Weinland, R.F., *et al*. (1919) *Berichte der deutschen chemischen Gesellschaft (A and B Series)*, **52**, 1316.
90. Kobayashi, A., *et al*. (1972) *Acta Crystallogr. B*, **28**, 3446.
91. Ryschkewitsch, G.E., *et al*. (1968) *J. Am. Chem. Soc.*, **90**, 7234.
92. Lemus, L., *et al*. (2013) *Dalton Trans.*, **42**, 11426.
93. Allcock, H.R., *et al*. (1973) *J. Am. Chem. Soc.*, **95**, 3154.
94. Cavezzan, J., *et al*. (1979) *Tetrahedron Lett.*, **20**, 795.
95. Shevchenko, I.V., *et al*. (1992) *Chemische Berichte*, **125**, 1325.
96. a) Gruselle, M., *et al*. (2004) *Mendeleev Commun.*, **14**, 282; b) Lacour, J., *et al*. (2000) *Angew. Chem. Int. Ed.*, **39**, 3695; c) Lacour, J., *et al*. (1998) *Chem. Commun.*, 1733; d) Naim, A., *et al*. (2018) *Inorg. Chem.*, **57**, 14501.
97. Matsuura, T., *et al*. (2005) *J. Photochem. Photobiol. C Photochem. Rev.*, **6**, 7.
98. Winkelmann, A., *et al*. (2015) *Ultramicroscopy*, **149**, 58.
99. Vogl, O. (2011) *J. Polym. Sci. A Poly. Chem.*, **49**, 1299.
100. Bunn, C.W., *et al*. (1954) *Nature*, **174**, 549.
101. a) Clark, E.S. (1999) *Polymer*, **40**, 4659; b) Farmer, B.L., *et al*. (1981) *Polymer*, **22**, 1487; c) Iwasaki, M. (1963) *J. Polym. Sci. A Gen. Pap.*, **1**, 1099; d) Matsushige, K., *et al*. (1977) *Jpn. J. Appl. Phys.*, **16**, 681; e) Weeks, J.J., *et al*. (1981) *Polymer*, **22**, 1480; f) Yamamoto, T. (1985) *J. Polym. Sci. Polym. Phys. Edn*, **23**, 771; g) Yamamoto, T., *et al*. (1986) *Polymer*, **27**, 986.
102. Pauling, L., *et al*. (1951) *Proc. Nat. Acad. Sci. U.S.A.*, **37**, 205.
103. Watson, J.D., *et al*. (1953) *Nature*, **171**, 737.

104. Natta, G., *et al*. (1955) *J. Am. Chem. Soc.*, **77**, 1708.
105. Tadokoro, H. (1979) *Die Makromolekulare Chemie*, **2**, 155.
106. a) Farina, M., *et al*. (1965) *Angew. Chem. Int. Ed.*, **4**, 107; b) Okamoto, Y., *et al*. (1994) *Chem. Rev.*, **94**, 349.
107. Nolte, R.J.M., *et al*. (1974) *J. Am. Chem. Soc.*, **96**, 5932.
108. Okamoto, Y., *et al*. (1979) *J. Am. Chem. Soc.*, **101**, 4763.
109. a) Cornelissen, J.J.L.M., *et al*. (2001) *Chem. Rev.*, **101**, 4039; b) Nakano, T., *et al*. (2001) *Chem. Rev.*, **101**, 4013; c) Yashima, E., *et al*. (2009) *Chem. Rev.*, **109**, 6102.
110. a) Brunsveld, L., *et al*. (2001) *Chem. Rev.*, **101**, 4071; b) Liu, M., *et al*. (2015) *Chem. Rev.*, **115**, 7304; c) Yashima, E., *et al*. (2016) *Chem. Rev.*, **116**, 13752; d) Ariga, K., *et al*. (2020) *Adv. Mater.*, **32**, 1905657.
111. Yang, F., *et al*. (2020) *Chem. Rev.*, **120**, 2693.
112. a) Watanabe, K., *et al*. (2012) *Chem. Mater.*, **24**, 1011, https://doi.org/10.1021/cm2028788; b) San Jose, B. A., *et al*. (2012) *J. Am. Chem. Soc.*, **134**, 19795, https://doi.org/10.1021/ja3086565; c) Nagata, Y., *et al*. (2014) *J. Am. Chem. Soc.*, **136**, 9858, https://doi.org/10.1021/ja504808r
113. a) Oda, M., *et al*. (2002) *Macromolecules*, **35**, 6792, https://doi.org/10.1021/ma020630g; b) Zawadzka, A., *et al*. (2019) *Opt. Mater.*, **96**, 109295, https://www.sciencedirect.com/science/article/pii/S0925346719305051
114. a) Janas, D., *et al*. (2017) *Mater. Des.*, **121**, 119, https://www.sciencedirect.com/science/article/pii/S0264127517301971; b) Krukiewicz, K., *et al*. (2018) *RSC Adv.*, **8**, 30600, http://dx.doi.org/10.1039/C8RA03963A
115. Akagi, K. (1998) *Science*, **282**, 1683.
116. Akagi, K. (2019) *Bull. Chem. Soc. Jpn.*, **92**, 1509.
117. Manaka, T., *et al*. (2006) *Chem. Lett.*, **35**, 1028.
118. Wu, S.-T., *et al*. (2014) *Angew. Chem. Int. Ed.*, **53**, 12860.
119. Maeda, K., *et al*. (2005) *Chem. Commun.*, 4152.
120. a) Guo, H., *et al*. (1999) *Synth. Met.*, **101**, 44; b) Huang, J., *et al*. (2003) *Adv. Mater.*, **15**, 1158.
121. a) Buono, A.M., *et al*. (2007) *J. Am. Chem. Soc.*, **129**, 10992; b) Guadagno, L., *et al*. (2008) *J. Mater. Chem.*, **18**, 567.
122. Rizzo, P., *et al*. (2011) *J. Am. Chem. Soc.*, **133**, 9872.
123. a) Guerra, G., *et al*. (2012) *J. Polym. Sci. B: Polym. Phys.*, **50**, 305; b) Guerra, G., *et al*. (2013) *Rendiconti Lincei*, **24**, 217; c) Rizzo, P., *et al*. (2016) *Chirality*, **28**, 29.
124. Nakano, T. (2014) *Chem. Rec.*, **14**, 369.
125. Iftime, G., *et al*. (2000) *J. Am. Chem. Soc.*, **122**, 12646.
126. Wang, Y., *et al*. (2012) *Chem. Commun.*, **48**, 1871.
127. Fujiki, M., *et al*. (2015) *Polym. Chem.*, **6**, 1627.
128. Miyata, M., *et al*. (2014) *Chem. Lett.*, **43**, 1476.
129. Simonyi, M., *et al*. (2003) *Chirality*, **15**, 680.
130. Bartik, K., *et al*. (2000) *ChemPhysChem*, **4**, 221.
131. Graf, E., *et al*. (1997) *Chem. Commun.*, 1459.

132. Okazaki, Y., *et al*. (2018) *Chem. Commun.*, **54**, 10244, https://hal.archives-ouvertes.fr/hal-02322340files/27/hal-02322340.html
133. Bleschke, C., *et al*. (2011) *Adv. Synth. Catal.*, **353**, 3101.
134. Ono, Y., *et al*. (1998) *Chem. Commun.*, **1477**.
135. a) Kelly, J.A., *et al*. (2014) *Acc. Chem. Res.*, **47**, 1088; b) Marx, S., *et al*. (2007) *Acc. Chem. Res.*, **40**, 768; c) Qiu, H., *et al*. (2011) *Chem. Soc. Rev.*, **40**, 1259; d) van Bommel, K. J. C., *et al*. (2003) *Angew. Chem. Int. Ed.*, **42**, 980.
136. Okazaki, Y., *et al*. (2016) *Nano Lett.*, **16**, 6411, https://doi.org/10.1021/acs.nanolett.6b02858files/51/acs.nanolett.html
137. a) Florescu, M., *et al*. (2009) *Phys. Rev. B*, **80**, 155112; b) Rechtsman, M.C., *et al*. (2008) *Phys. Rev. Lett.*, **101**, 073902.
138. Sholl, D.S., *et al*. (2001) *J. Phys. Chem. B*, **105**, 4771.
139. Chen, Y., *et al*. (2020) *Phys. Rev. Lett.*, **235502**.
140. Konevtsova, O.V., *et al*. (2012) *Phys. Rev. Lett.*, **108**, 038102.
141. Toda, F. (2004) *Enantiomer Separation*, Springer Netherlands.
142. a) Stinson, S.C. (2001) *Chem. Eng. News Arch.*, **79**, 45, https://doi.org/10.1021/cen-v079n020.p045; b) Wagnière, G.H. (2008). *On Chirality and the Universal Asymmetry: Reflections on Image and Mirror Image*, Wiley-Verlag Helvetica Chimica Acta.
143. Smith, S.W. (2009) Toxicological Sciences **110**, 4. https://doi.org/10.1093/toxsci/kfp097
144. Jozwiak, K., Lough, W.J., and Wainer, I.W. (2012) *Drug Stereochemistry* 3ed., CRC Press.
145. De Camp, W.H. (1989) *Chirality*, **1**, 2, https://doi.org/10.1002/chir.530010103
146. a) Chang, C., *et al*. (2012) *TrAC Trends Anal. Chem.*, **39**, 195, https://www.sciencedirect.com/science/article/pii/S0165993612001951; b) Gogoi, A.A.-O., *et al*. (2019) *Molecules*, 24, 1007; doi: 10.3390/molecules24061007; c) Maier, N.M., *et al*. (2001) *J. Chromatogr. A*, **906**, 3, https://www.sciencedirect.com/science/article/pii/S002196730000532X
147. Francotte, E. (2009) *Chimia (Aarau)*, **63**, 867, http://europepmc.org/abstract/MED/28372616; https://doi.org/10.2533/chimia.2009.867
148. Blaser, H.-U., *et al*. (2005) *J. Mol. Catal. A Chem.*, **231**, 1, https://www.sciencedirect.com/science/article/pii/S1381116904009057
149. a) Schuur, B., *et al*. (2011) *Org. Biomol. Chem.*, **9**, 36, http://dx.doi.org/10.1039/C0OB00610F; b) Steensma, M., *et al*. (2006) *Chirality*, **18**, 314, https://doi.org/10.1002/chir.20258
150. a) Ahuja, S. (2001) *Org. Process. Res. Dev.*, **5**, 458, https://doi.org/10.1021/op0100293; b) Hazen, R.M., *et al*. (2003) *Nat. Mater.*, **2**, 367; c) Lang, J.C., *et al*. (2017) *Curr. Opin. Colloid Interface Sci.*, **32**, 94, https://www.sciencedirect.com/science/article/pii/S1359029417301413
151. a) Horvath, J.D., *et al*. (2004) *J. Am. Chem. Soc.*, **126**, 14988, https://doi.org/10.1021/ja045537h; b) Yun, Y., *et al*. (2013) *Angew. Chem. Int. Ed.*, **52**, 3394, https://doi.org/10.1002/anie.201209025; c) Yun, Y., *et al*. (2015) *Langmuir*, **31**, 6055, https://doi.org/10.1021/acs.langmuir.5b00707

152. a) de Alwis, A., *et al*. (2013) *Surf. Sci.*, **608**, 80, https://www.sciencedirect.com/science/article/pii/S0039602812003457; b) Karagoz, B., *et al*. (2019) *Langmuir*, **35**, 16438, https://doi.org/10.1021/acs.langmuir.9b02476
153. Halasyamani, P.S., *et al*. (1998) *Chem. Mater.*, **10**, 2753.
154. a) Karagunis, G., *et al*. (1938) *Nature*, **142**, 162; b) Tsuchida, R., *et al*. (1936) *Bull. Chem. Soc. Jpn.*, **11**, 38.
155. a) Bonner, W.A., *et al*. (1974) *Science*, **186**, 143; b) Hartwig, B.A., *et al*. (1972) *J. Biomed. Mater. Res.*, **6**, 413.
156. Guevremont, J.M., *et al*. (1998) *Am. Mineral.*, **83**, 1246.
157. Jenkins, S.J., *et al*. (2007) *Surf. Sci. Rep.*, **62**, 373.
158. Cody, A.M., *et al*. (1991) *J. Cryst. Grow.*, **113**, 508.
159. Orme, C.A., *et al*. (2001) *Nature*, **411**, 775, https://doi.org/10.1038/35081034
160. Hazen, R.M., *et al*. (2001) *Proc. Nat. Acad. Sci. U.S.A.*, **98**, 5487.
161. a) Kelso, M.V., *et al*. (2018) *J. Am. Chem. Soc.*, **140**, 15812; b) McFadden, C. F., *et al*. (1996) *Langmuir*, **12**, 2483.
162. a) Kajioka, H., *et al*. (2010) *Macromolecules*, **43**, 3837; b) Toda, A., *et al*. (2003) *Polymer*, **44**, 6135; c) Toda, A., *et al*. (2005) *Polymer*, **46**, 8708.
163. Vand, V. (1951) *Nature*, **168**, 783.
164. a) Neuber, M., *et al*. (1995) *J. Phys. Chem.*, **99**, 9160; b) Raval, R. (2009) *Chem. Soc. Rev.*, **38**, 707.
165. a) Kauranen, M., *et al*. (1994) *J. Chem. Phys.*, **101**, 8193; b) T. Petralli-Mallow, *et al*. (1993) *J. Phys. Chem.*, **97**, 1383; c) Verbiest, T., *et al*. (1994) *J. Am. Chem. Soc.*, **116**, 9203.
166. a) Attard, G.A. (2001) *J. Phys. Chem. B*, **105**, 3158, https://doi.org/10.1021/jp0041508; b) Attard, G.A., *et al*. (1999) *J. Phys. Chem. B*, **103**, 1381; c) Hazzazi, O.A., *et al*. (2004) *J. Mol. Catal. A Chem.*, **216**, 247.
167. a) Nakanishi, T., *et al*. (2002) *J. Am. Chem. Soc.*, **124**, 740; b) Nakanishi, T., *et al*. (2004) *Chirality*, **16**, S36.
168. a) Barlow, S.M., *et al*. (2003) *Surf. Sci. Rep.*, **50**, 201, https://www.sciencedirect.com/science/article/pii/S0167572903000153; b) Humblot, V., *et al*. (2004) *J. Am. Chem. Soc.*, **126**, 6460, https://doi.org/10.1021/ja0382056; c) Lorenzo, M.O., *et al*. (1999) *J. Phys. Chem. B*, **103**, 10661, https://doi.org/10.1021/jp992188i; d) Ohmann, R., *et al*. (2011) *ACS Nano*, **5**, 1360, https://doi.org/10.1021/nn103058e
169. a) Darling, G.R., *et al*. (2017) *Phys. Chem. Chem. Phys.*, **19**, 7617; b) Madden, D.C., *et al*. (2014) *Surf. Sci.*, **629**, 81, https://www.sciencedirect.com/science/article/pii/S0039602814000910; c) Madden, D.C., *et al*. (2014) *J. Phys. Chem. C*, **118**, 18589, https://doi.org/10.1021/jp505636v; d) Therrien, A.J., *et al*. (2016) *Chem. Commun.*, **52**, 14282, http://dx.doi.org/10.1039/C6CC05820E
170. a) Forster, M., *et al*. (2016) *Chem. Commun.*, **52**, 14075; b) Sleczkowski, P., *et al*. (2016) *J. Phys. Chem. C*, **120**, 22388, https://doi.org/10.1021/acs.jpcc.6b06800
171. Cun, H., *et al*. (2010) *Langmuir*, **26**, 3402, https://doi.org/10.1021/la903193a

172. a) Mateo Marti, E., *et al*. (2002) *Surf. Sci.*, **501**, 191, https://www.sciencedirect.com/science/article/pii/S003960280102026X; b) Yang, B., *et al*. (2010) *J. Am. Chem. Soc.*, **132**, 10440, https://doi.org/10.1021/ja102989y
173. a) Haq, S., *et al*. (2007) *Langmuir*, **23**, 10694, https://doi.org/10.1021/la700965d; b) Seibel, J., *et al*. (2015) *J. Am. Chem. Soc.*, **137**, 7970, https://doi.org/10.1021/jacs.5b02262
174. a) Chen, Q., *et al*. (2002) *Surf. Sci.*, **497**, 37, https://www.sciencedirect.com/science/article/pii/S003960280101593X; b) Liu, N., *et al*. (2011) *Chem. Commun.*, **47**, 11324, http://dx.doi.org/10.1039/C1CC13317A
175. Lopinski, G.P., *et al*. (1998) *Nature*, **392**, 909.
176. Booth, N.A., *et al*. (1998) *Surf. Sci.*, **397**, 258.
177. Weckesser, J., *et al*. (1999) *J. Chem. Phys.*, **110**, 5351.
178. a) Chen, Q., *et al*. (2003) *Nat. Mater.*, **2**, 324; b) A. McNutt, *et al*. (2003) *Surf. Sci.*, **531**, 131.
179. Gopakumar, T.G., *et al*. (2010) *J. Phys. Chem. C*, **114**, 18247.
180. a) Böhringer, M., *et al*. (1999) *Angew. Chem. Int. Ed.*, **38**, 821; b) Böhringer, M., *et al*. (1999) *Phys. Rev. Lett.*, **83**, 324.
181. France, C.B., *et al*. (2003) *J. Am. Chem. Soc.*, **125**, 12712.
182. Wei, Y., *et al*. (2004) *J. Am. Chem. Soc.*, **126**, 5318.
183. Schlickum, U., *et al*. (2008) *J. Am. Chem. Soc.*, **130**, 11778.
184. Barlow, S.M., *et al*. (2003) *Surf. Sci. Rep.*, **50**, 201.
185. a) Baiker, A. (2005) *Catal. Today*, **100**, 159, https://www.sciencedirect.com/science/article/pii/S0920586104007576; b) Zaera, F. (2008) *J. Phys. Chem. C*, **112**, 16196, https://doi.org/10.1021/jp804588v; c) Gross, E., *et al*. (2013) *J. Am. Chem. Soc.*, **135**, 3881, https://doi.org/10.1021/ja310640b
186. a) Núñez, O., *et al*. (2008) *J. Chromatogr. A*, **1191**, 231; b) Zhao, J., *et al*. (2015) *J. Chromatogr. A*, **1381**, 253, https://www.sciencedirect.com/science/article/pii/S0021967315000540
187. a) Jonkheijm, P., *et al*. (2008) *Angew. Chem. Int. Ed.*, **47**, 9618, https://doi.org/10.1002/anie.200801711; b) Mansur, H.S., *et al*. (2005) *J. Mater. Sci. Mater. Med.*, **16**, 333, https://doi.org/10.1007/s10856-005-0632-y; c) Welch, N.G., *et al*. (2017) *Biointerphases*, **12**, 02D301, https://doi.org/10.1116/1.4978435; d) Yu, Q., *et al*. (2015) *Crit. Rev. Anal. Chem.*, **45**, 62, https://doi.org/10.1080/10408347.2014.881249
188. a) Heitbaum, M., *et al*. (2006) *Angew. Chem. Int. Ed. Engl.*, **45**, 4732; b) P. McMorn, *et al*. (2004) *Chem. Soc. Rev.*, **33**, 108, http://dx.doi.org/10.1039/B200387M
189. Durán Pachón, L., *et al*. (2009) *Nat. Chem.*, **1**, 160, https://doi.org/10.1038/nchem.180
190. Woodruff, D.P. (2002) *Surf. Sci.*, **500**, 147, https://www.sciencedirect.com/science/article/pii/S0039602801015345
191. a) Gellman, A.J., *et al*. (2015) *Catal. Lett.*, **145**, 220, https://doi.org/10.1007/s10562-014-1400-8; b) Lawton, T.J., *et al*. (2013) *J. Phys. Chem. C*, **117**, 22290, https://doi.org/10.1021/jp402015r

192. a) Behar-Levy, H., *et al*. (2002) *Chem. Mater.*, **14**, 1736, https://doi.org/10.1021/cm011558o; b) Nesher, G., *et al*. (2008) *Chem. Mater.*, **20**, 4425, https://doi.org/10.1021/cm800657j; c) Yosef, I., *et al*. (2006) *Chem. Mater.*, **18**, 5890, https://doi.org/10.1021/cm0615368
193. a) H. Behar-Levy, *et al*. (2007) *Adv. Mater.*, **19**, 1207, https://doi.org/10.1002/adma.200601702; b) Goldsmith, M.-R., *et al*. (2006) *Phys. Chem. Chem. Phys.*, **8**, 63, http://dx.doi.org/10.1039/B511563A; c) Yang, H., *et al*. (2014) *Chem. Commun.*, **50**, 8868, http://dx.doi.org/10.1039/C4CC02823F
194. Bohannan, E.W., *et al*. (2004) *J. Am. Chem. Soc.*, **126**, 488, https://doi.org/10.1021/ja039422+
195. a) Fang, Y., *et al*. (2017) *ChemElectroChem*, **4**, 1832, https://doi.org/10.1002/celc.201700257; b) Wattanakit, C., *et al*. (2014) *Nat. Commun.*, **5**, 3325, https://doi.org/10.1038/ncomms4325
196. a) Kothari, H.M., *et al*. (2004) *Chem. Mater.*, **16**, 4232, https://doi.org/10.1021/cm048939x; b) Switzer, J.A., *et al*. (2003) *Nature*, **425**, 490, https://doi.org/10.1038/nature01990
197. Gautier, C., *et al*. (2009) *ChemPhysChem*, **10**, 483, https://doi.org/10.1002/cphc.200800709 https://chemistry-europe.onlinelibrary.wiley.com/doi/pdfdirect/10.1002/cphc.200800709?download=true
198. Ma, W., *et al*. (2017) *Chem. Rev.*, **117**, 8041, https://doi.org/10.1021/acs.chemrev.6b00755
199. a) Gautier, C., *et al*. (2008) *J. Am. Chem. Soc.*, **130**, 7077, https://www.ncbi.nlm.nih.gov/pubmed/18459786; b) Schaaff, T.G., *et al*. (2000) *J. Phys. Chem. B*, **104**, 2630.
200. Li, T., *et al*. (2004) *Nanotechnology*, **15**, S660.
201. Yao, H., *et al*. (2005) *J. Am. Chem. Soc.*, **127**, 15536.
202. a) Gautier, C., *et al*. (2006) *J. Am. Chem. Soc.*, **128**, 11079, https://www.ncbi.nlm.nih.gov/pubmed/16925425; b) Ock, K.S., *et al*. (2013) *Spectrochim. Acta A Mol. Biomol. Spectrosc.*, **102**, 419, https://www.ncbi.nlm.nih.gov/pubmed/23261512
203. Moloney, M.P., *et al*. (2007) *Chem. Commun.*, 3900, https://www.ncbi.nlm.nih.gov/pubmed/17896026
204. Nakashima, T., *et al*. (2009) *J. Am. Chem. Soc.*, **131**, 10342, https://www.ncbi.nlm.nih.gov/pubmed/19588974
205. Mukhina, M.V., *et al*. (2015) *Nano Lett.*, **15**, 2844, http://www.ncbi.nlm.nih.gov/pubmed/25908405
206. Choi, J.K., *et al*. (2016) *ACS Nano*, **10**, 3809, http://www.ncbi.nlm.nih.gov/pubmed/26938741
207. Kuno, J., *et al*. (2018) *Angew. Chem. Int. Ed. Engl.*, **57**, 12022, https://www.ncbi.nlm.nih.gov/pubmed/30054963
208. Kuznetsova, V.A., *et al*. (2019) *ACS Nano*, **13**, 13560, <Go to ISI>://WOS:000500650000129
209. Zhou, Y., *et al*. (2011) *Angew. Chem. Int. Ed. Engl.*, **50**, 11456, http://www.ncbi.nlm.nih.gov/pubmed/22113805

210. Moshe, A.B., *et al*. (2011) *ACS Nano*, **5**, 9034, https://www.ncbi.nlm.nih.gov/pubmed/21967095
211. Gao, X., *et al*. (2017) *J. Am. Chem. Soc.*, **139**, 8734, http://www.ncbi.nlm.nih.gov/pubmed/28582623
212. a) Cheng, J., *et al*. (2018) *ACS Nano*, **12**, 5341, http://www.ncbi.nlm.nih.gov/pubmed/29791135; b) Hao, J., *et al*. (2020) *ACS Nano*, **14**, 10346, https://pubs.acs.org/doi/pdf/10.1021/acsnano.0c03909; c) Shao, X., *et al*. (2020) *Inorg. Chem.*, **59**, 14382, https://www.ncbi.nlm.nih.gov/pubmed/32945662
213. Gao, X., *et al*. (2018) *Nano Lett.*, **18**, 6665, http://www.ncbi.nlm.nih.gov/pubmed/30350652
214. Purcell-Milton, F., *et al*. (2017) *ACS Nano*, **11**, 9207.
215. a) Chen, C., *et al*. (2019) *Nat. Commun.*, **10**, 1927, https://www.ncbi.nlm.nih.gov/pubmed/31028272; b) Chen, W., *et al*. (2019) *J. Phys. Chem. Lett.*, **10**, 3290, http://www.ncbi.nlm.nih.gov/pubmed/31146530; c) He, T., *et al*. (2017) *Appl. Phys. Lett.*, **111**, 151102; d) Long, G., *et al*. (2020) *Nat. Rev. Mater.*, **5**, 423.
216. Jiang, W., *et al*. (2019) *Mater. Horiz.*, **6**, 1974, http://dx.doi.org/10.1039/C9MH00431A
217. a) Che, S., *et al*. (2003) *Nat. Mater.*, **2**, 801, https://www.ncbi.nlm.nih.gov/pubmed/14634644; b) Delclos, T., *et al*. (2008) *Nano Lett.*, **8**, 1929, https://doi.org/10.1021/nl080664nfiles/128/nl080664n.html; c) Paredes, B., *et al*. (2004) *Nature*, **429**, 277, https://www.ncbi.nlm.nih.gov/pubmed/15152247; d) Sugiyasu, K., *et al*. (2002) *Chem. Commun.*, **1212**.
218. Liu, S., *et al*. (2012) *Nat. Commun.*, **3**, 1215, https://www.ncbi.nlm.nih.gov/pubmed/23169056
219. Duan, Y., *et al*. (2015) *Angew. Chem. Int. Ed. Engl.*, **54**, 15170, https://www.ncbi.nlm.nih.gov/pubmed/26489386
220. Sone, E.D., *et al*. (2002) *Angew. Chem. Int. Ed.*, **41**, 1705, https://onlinelibrary.wiley.com/doi/pdfdirect/10.1002/1521-3773%2820020517%2941%3A10%3C1705%3A%3AAID-ANIE1705%3E3.0.CO%3B2-M?download=true
221. Ma, L., *et al*. (2017) *Angew. Chem. Int. Ed. Engl.*, **56**, 8657, https://www.ncbi.nlm.nih.gov/pubmed/28544063
222. Duan, Y., *et al*. (2014) *J. Am. Chem. Soc.*, **136**, 7193, https://www.ncbi.nlm.nih.gov/pubmed/24802633
223. Wu, Y.-J., *et al*. (2012) *Cryst. Growth Des.*, **12**, 547, https://doi.org/10.1021/cg201246m
224. Jiang, W., *et al*. (2017) *Nat. Commun.*, **8**, 1.
225. Ben-Moshe, A., *et al*. (2014) *Nat. Commun.*, **5**, 4302, http://www.ncbi.nlm.nih.gov/pubmed/25001884
226. a) Wang, P.P., *et al*. (2017) *Nat. Commun.*, **8**, 14312, http://www.ncbi.nlm.nih.gov/pubmed/28148957; b) Wang, P.P., *et al*. (2017) *J. Am. Chem. Soc.*, **139**, 6070, http://www.ncbi.nlm.nih.gov/pubmed/28414901

227. Lee, H.E., *et al*. (2018) *Nature*, **556**, 360, https://www.ncbi.nlm.nih.gov/pubmed/29670265
228. a) Cho, N.H., *et al*. (2020) *ACS Nano*, **14**, 3595, https://www.ncbi.nlm.nih.gov/pubmed/32134639; b) Karst, J., *et al*. (2019) *ACS Nano*, **13**, 8659, https://www.ncbi.nlm.nih.gov/pubmed/31294546; c) Kim, H., *et al*. (2020) *Angew. Chem. Int. Ed. Engl.*, **59**, 12976, https://www.ncbi.nlm.nih.gov/pubmed/32337812; d) Yuan, C., *et al*. (2019) *J. Nanosci. Nanotechnol.*, **19**, 2789, http://www.ncbi.nlm.nih.gov/pubmed/30501781
229. Cho, N.H., *et al*. (2019) *Part. Part. Syst. Characterizat.*, **36**.
230. a) Glotzer, S.C. (2004) *Science*, **306**, 419; b) Glotzer, S.C., *et al*. (2007) *Nat. Mater.*, **6**, 557, http://dx.doi.org/10.1038/nmat1949; c) Velev, O.D., *et al*. (2009) *Adv. Mater.*, **21**, 1897; d) Zhang, X., *et al*. (2016) *Adv. Mater.*, **28**, 2475, https://doi.org/10.1002/adma.201504206
231. Blell, R., *et al*. (2017) *ACS Nano*, **11**, 84, https://doi.org/10.1021/acsnano.6b04191
232. Liu, J.-W., *et al*. (2012) *Chem. Rev.*, **112**, 4770.
233. Faustini, M., *et al*. (2010) *J. Phys. Chem. C*, **114**, 7637.
234. a) Han, W., *et al*. (2012) *Angew. Chem. Int. Ed.*, **51**, 1534, https://onlinelibrary.wiley.com/doi/abs/10.1002/anie.201104454; b) Huang, J., *et al*. (2007) *Angew. Chem. Int. Ed.*, **46**, 2414, https://onlinelibrary.wiley.com/doi/abs/10.1002/anie.200604789; c) Petty, M.C. (1992) *Thin Solid Films*, **210–211**, 417, https://www.sciencedirect.com/science/article/pii/004060909290300Z
235. a) Hu, H., *et al*. (2017) *Nanoscal*; b) Huang, Y., *et al*. (2001) *Science*, **291**, 630, https://science.sciencemag.org/content/sci/291/5504/630.full.pdf
236. a) Sarker, B.K., *et al*. (2011) *ACS Nano*, **5**, 6297, https://doi.org/10.1021/nn201314t; b) Wang, B., *et al*. (2010) *Adv. Mater.*, **22**, 3067, https://onlinelibrary.wiley.com/doi/abs/10.1002/adma.201000705; c) Xie, J., *et al*. (2008) *Macromol. Rapid Commun.*, **29**, 1775, https://onlinelibrary.wiley.com/doi/abs/10.1002/marc.200800381
237. a) Hangarter, C.M., *et al*. (2007) *Nanotechnology*, **18**, 205305; b) Shklyarevskiy, I.O., *et al*. (2005) *Langmuir*, **21**, 2108, https://doi.org/10.1021/la047166o
238. a) Jin, L., *et al*. (1998) *Appl. Phys. Lett.*, **73**, 1197, https://aip.scitation.org/doi/abs/10.1063/1.122125; b) Zhang, S., *et al*. (2014) *Biomaterials*, **35**, 3243, https://www.sciencedirect.com/science/article/pii/S0142961213015779
239. Xu, C.Y., *et al*. (2004) *Biomaterials*, **25**, 877, https://www.sciencedirect.com/science/article/pii/S0142961203005933
240. a) Dugyala, V.R., *et al*. (2015) *RSC Adv.*, **5**, 60079; b) Li, P., *et al*. (2016) *Adv. Mater.*, **28**, 2511; c) Srikantharajah, R., *et al*. (2016) *Nanoscale*, **8**, 19882.
241. Singh, G., *et al*. (2014) *Science*, **345**, 1149, https://www.ncbi.nlm.nih.gov/pubmed/25061133
242. Jana, S., *et al*. (2017) *Sci. Adv.*, **3**, e1701483, https://www.ncbi.nlm.nih.gov/pubmed/28924613
243. Yin, Y., *et al*. (2003) *J. Am. Chem. Soc.*, **125**, 2048, https://www.ncbi.nlm.nih.gov/pubmed/12590523

244. a) Bishop, K.J., *et al*. (2009) *Small*, **5**, 1600, http://www.ncbi.nlm.nih.gov/pubmed/19517482; b) Boles, M.A., *et al*. (2016) *Chem. Rev.*, **116**, 11220, http://www.ncbi.nlm.nih.gov/pubmed/27552640
245. Srivastava, S., *et al*. (2010) *Science*, **327**, 1355, https://www.ncbi.nlm.nih.gov/pubmed/20150443
246. Yeom, J., *et al*. (2015) *Nat. Mater.*, **14**, 66, http://www.ncbi.nlm.nih.gov/pubmed/25401922
247. Kim, J.Y., *et al*. (2019) *J. Am. Chem. Soc.*, **141**, 11739, https://www.ncbi.nlm.nih.gov/pubmed/31329438
248. Feng, W., *et al*. (2017) *Sci. Adv.*, 3, e1601159, https://www.ncbi.nlm.nih.gov/pmc/articles/PMC5332156/pdf/1601159.pdf
249. Zhou, Y., *et al*. (2016) *ACS Nano*, **10**, 3248, http://www.ncbi.nlm.nih.gov/pubmed/26900920
250. Yan, J., *et al*. (2019) *Chem. Mater.*, **32**, 476.
251. Jiang, W., *et al*. (2020) *Science*, eaaz7949, https://science.sciencemag.org/content/sci/early/2020/04/08/science.aaz7949.full.pdf
252. a) Kuncicky, D.M., *et al*. (2006) *Small*, **2**, 1462; b) Wargacki, S.P., *et al*. (2008) *Langmuir*, **24**, 5439, https://doi.org/10.1021/la7040778
253. a) Dumanli, A.G., *et al*. (2014) *ACS Appl. Mater. Interfaces*, **6**, 12302, https://doi.org/10.1021/am501995e; b) Tran, A., *et al*. (2020) *Adv. Mater.*, **32**, 1905876, https://onlinelibrary.wiley.com/doi/abs/10.1002/adma.201905876
254. Cherpak, V., *et al*. (2018) *Nano Lett.*, **18**, 6770, https://doi.org/10.1021/acs.nanolett.8b02522
255. Gao, J., *et al*. (2019) *Chem. Mater.*, **32**, 821.
256. a) Dietrich, K., *et al*. (2012) *Adv. Mater.*, 24, OP321, https://onlinelibrary.wiley.com/doi/abs/10.1002/adma.201203424; b) Zhao, Y., *et al*. (2012) *Nat. Commun.*, **3**, 870, https://doi.org/10.1038/ncomms1877
257. Urban, M.J., *et al*. (2019) *Annu. Rev. Phys. Chem.*, **70**, 275.
258. a) Liang, Z., *et al*. (2016) *Faraday Discuss.*, **191**, 141, http://dx.doi.org/10.1039/C6FD00064A; b) Gao, J., *et al*. (2020) *ACS Nano*, **14**, 4111.
259. Gil Perez, J.J., *et al*. (2016) *Polarized Light and the Mueller Matrix Approach,* CRC Press.
260. a) Arteaga, O., *et al*. (2012) *Appl. Opt*., **51**, 6805, http://ao.osa.org/abstract.cfm?URI=ao-51-28-6805; b) Azzam, R.M.A. (1978) *J. Opt. Soc. Am.*, **68**, 1756, http://www.osapublishing.org/abstract.cfm?URI=josa-68-12-1756; c) Cloude, S. (1990) *Conditions for the Physical Realisability of Matrix Operators in Polarimetry*, Vol. 1166, 177 SPIE; d) Lu, S.-Y., *et al*. (1996) *J. Opt. Soc. Am. A*, **13**, 1106, http://josaa.osa.org/abstract.cfm?URI=josaa-13-5-1106
261. Drake, A.F. (1986) *J. Phys. E Sci. Instrum.*, **19**, 170, http://dx.doi.org/10.1088/0022-3735/19/3/002
262. Nafie, L.A., *et al*. (1982) *Techniques Using Fourier Transform Interferometry*, Vol. 3, Elsevier.

263. a) Modine, F.A., *et al*. (1975) *Appl. Opt.*, **14**, 761, http://ao.osa.org/abstract.cfm?URI=ao-14-3-761; b) Shindo, Y., *et al*. (1989) *Rev. Sci. Instrum.*, **60**, 3633, https://doi.org/10.1063/1.1140467
264. a) Disch, R.L., *et al*. (1969) *Anal. Chem.*, **41**, 82, https://doi.org/10.1021/ac60270a038; b) Shindo, Y., *et al*. (1990) *Biopolymers*, **30**, 405, https://doi.org/10.1002/bip.360300318
265. Buffeteau, T., *et al*. (2005) Appl. Spectroscopy, 59, 732, https://doi.org/10.1366/0003702054280568
266. Collins, R.W., *et al*. (1999) *J. Opt. Soc. Am. A*, **16**, 1997, http://josaa.osa.org/abstract.cfm?URI=josaa-16-8-1997
267. De Martino, A., *et al*. (2003) *Opt. Lett.*, **28**, 616, http://ol.osa.org/abstract.cfm?URI=ol-28-8-616
268. Jellison, J., *et al*., *Two Modulator Generalized Ellipsometer for Complete Mueller Matrix Measurement*, **5956147**.
269. a) Arwin, H., *et al*. (2019) *J. Vac. Sci. Technol. B*, **38**, 014004, https://doi.org/10.1116/1.5131634; b) A. Mendoza-Galván, *et al*. (2018) *J. Opt.*, **20**, 024001, http://dx.doi.org/10.1088/2040-8986/aa9e7d
270. a) Nikolas, J.P., *et al*. (2008) *J. Nanophotonics*, **2**, 1, https://doi.org/10.1117/1.3062210; b) Oates, T.W.H., *et al*. (2014) *Opt. Mater. Express*, **4**, 2646, http://www.osapublishing.org/ome/abstract.cfm?URI=ome-4-12-2646